Geophysical Journal International

Geophys. J. Int. (2019) **216,** 61–80
Advance Access publication 2018 September 06
GJI Seismology

doi: 10.1093/gji/ggy368

The importance of including density in elastic least-squares reverse time migration: multiparameter crosstalk and convergence

Ke Chen and Mauricio D. Sacchi

Department of Physics, University of Alberta, Edmonton, AB T6G 2E1, Canada. E-mail: ke7@ualberta.ca

Accepted 2018 September 5. Received 2018 July 31; in original form 2018 February 10

SUMMARY

Time-domain elastic least-squares reverse time migration (LSRTM) can provide higher spatial resolution images with fewer artefacts and a superior balance of amplitudes than elastic reverse time migration (RTM). More important, it can mitigate the crosstalk between *P*- and *S*-wave images. In previously proposed elastic LSRTM algorithms, density is either assumed to be constant or known. In other words, the density perturbation is not part of the least-squares inversion formulation. Neglecting density in elastic LSRTM may lead to crosstalk artefacts in the *P*- and *S*-wave images. In this paper, we propose a time-domain three-parameter elastic LSRTM algorithm to simultaneously invert for density, *P*- and *S*-wave velocity perturbation images. We derive the elastic Born approximation and elastic RTM operators using the continuous adjoint-state method. We carefully discretize the two operators to assure that they pass the dot-product test. This allows us to use the conjugate gradient least-squares method to solve the least-squares migration problem. We evaluate the proposed algorithm on two synthetic examples. We show that our proposed three-parameter elastic LSRTM can suppress the multiparameter crosstalk among density, *P*- and *S*-wave velocity perturbation images. Moreover, including density image in the elastic LSRTM inversion can improve the convergence of the least-squares inversion.

Key words: Inverse theory; Waveform inversion; Computational seismology; Seismic tomography; Wave propagation.

INTRODUCTION

Seismic imaging techniques aim at portraying subsurface structure using seismic data. Reverse time migration (RTM; Baysal *et al.* 1983; McMechan 1983; Whitmore 1983; Etgen 1986; Zhang & Sun 2009; Li & Chauris 2017) is one of the most important seismic imaging methods. RTM utilizes the two-way acoustic wave equation for extrapolating wavefields into the interior of the Earth. For this reason, RTM can handle steep and complex geological structures such as sedimentary areas with salt inclusions (Etgen *et al.* 2009). Due to the rapid development of computing power, RTM has become one of the most popular methods for industry applications of imaging techniques for resource exploration and exploitation. Acoustic RTM methods approximate the elastic solid Earth by a fluid. However, an elastic formulation provides a better approximation to realistic media at exploration scales. Different elastic RTM methods have been developed by applying the excitation-time imaging condition (Sun & McMechan 1986; Chang & McMechan 1987; Sun & McMechan 2001), the cross-correlation imaging condition (Yan & Sava 2008; Du *et al.* 2012) or utilizing elastic full-waveform inversion gradients (Tarantola 1986; Tromp *et al.* 2005; Fichtner *et al.* 2006a,b; Fichtner 2010).

The migrated images may suffer from relative low spatial resolution, unbalanced amplitudes due to geometric spreading and acquisition footprint. Those issues can be mitigated by the least-squares migration (LSM). Different LSM techniques have been proposed in seismic imaging: least-squares Kirchhoff migration (Tarantola 1984; Lambare *et al.* 1992; Nemeth *et al.* 1999; Trad 2015, 2017), least-squares one-way wave equation migration (Kuehl & Sacchi 2003; Rickett 2003; Wang *et al.* 2005; Tang 2009; Kaplan *et al.* 2010; Kazemi & Sacchi 2015; Cheng *et al.* 2016) and least-squares reverse time migration (LSRTM; Bourgeois *et al.* 1989; Ostmo *et al.* 2002; Dai *et al.* 2012; Dong *et al.* 2012; Zhang *et al.* 2015; Hou & Symes 2016; Xue *et al.* 2016; Yang *et al.* 2016; Yao & Jakubowicz 2016; Chen *et al.* 2017; Xu & Sacchi 2018). For inverting multicomponent data, elastic LSM methods

© The Author(s) 2018. Published by Oxford University Press on behalf of The Royal Astronomical Society.

Downloaded from https://academic.oup.com/gji/article-abstract/216/1/61/5091812 by University of California, Berkeley/LBL user on 21 June 2019

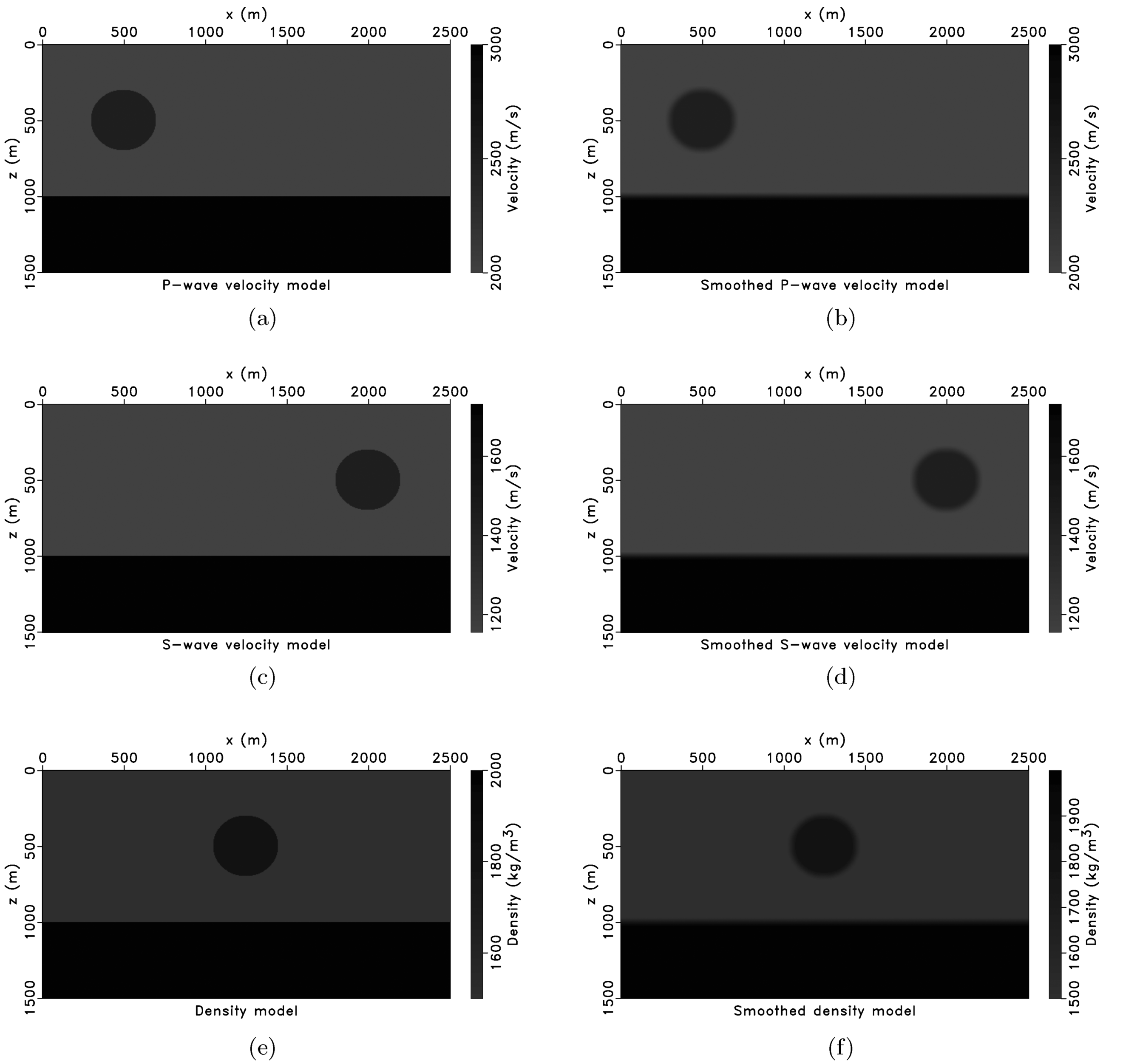

Figure 1. Elastic inclusion model. (a) *P*-wave velocity model. (b) Smoothed *P*-wave velocity model. (c) *S*-wave velocity model. (d) Smoothed *S*-wave velocity model. (e) Density model. (f) Smoothed density model.

have also been developed. For example, elastic least-squares Kirchhoff migration (Beydoun & Mendes 1989; Jin *et al.* 1992), elastic least-squares one-way wave equation migration (Stanton & Sacchi 2015, 2017), and elastic LSRTM (Anikiev *et al.* 2013; Xu *et al.* 2016; Chen & Sacchi 2017; Duan *et al.* 2017; Feng & Schuster 2017; Gu *et al.* 2017; Ren *et al.* 2017; Guo & McMechan 2018).

Conventional elastic LSRTM algorithms do not include density image in the inversion. It inverts for *P*- and *S*-wave images. We call this type of elastic LSRTM a two-parameter elastic LSRTM. The density is either assumed to be constant or already known. However, this assumption is not valid in realistic Earth media. Neglecting the density image in elastic LSRTM may result in crosstalk artefacts in the *P*- and *S*-wave images. Chen & Sacchi (2017) derive an elastic LSRTM algorithm including the density image component. However, they did not include density image inversion in their numerical examples. Sun *et al.* (2017) study a frequency-domain elastic LSRTM with density variation. Qu *et al.* (2018) present an elastic LSRTM with density variation based on *P*- and *S*-wave decoupled elastic velocity-stress wave equation. In this paper, we

Downloaded from https://academic.oup.com/gji/article-abstract/216/1/61/5091812 by University of California, Berkeley/LBL user on 21 June 2019

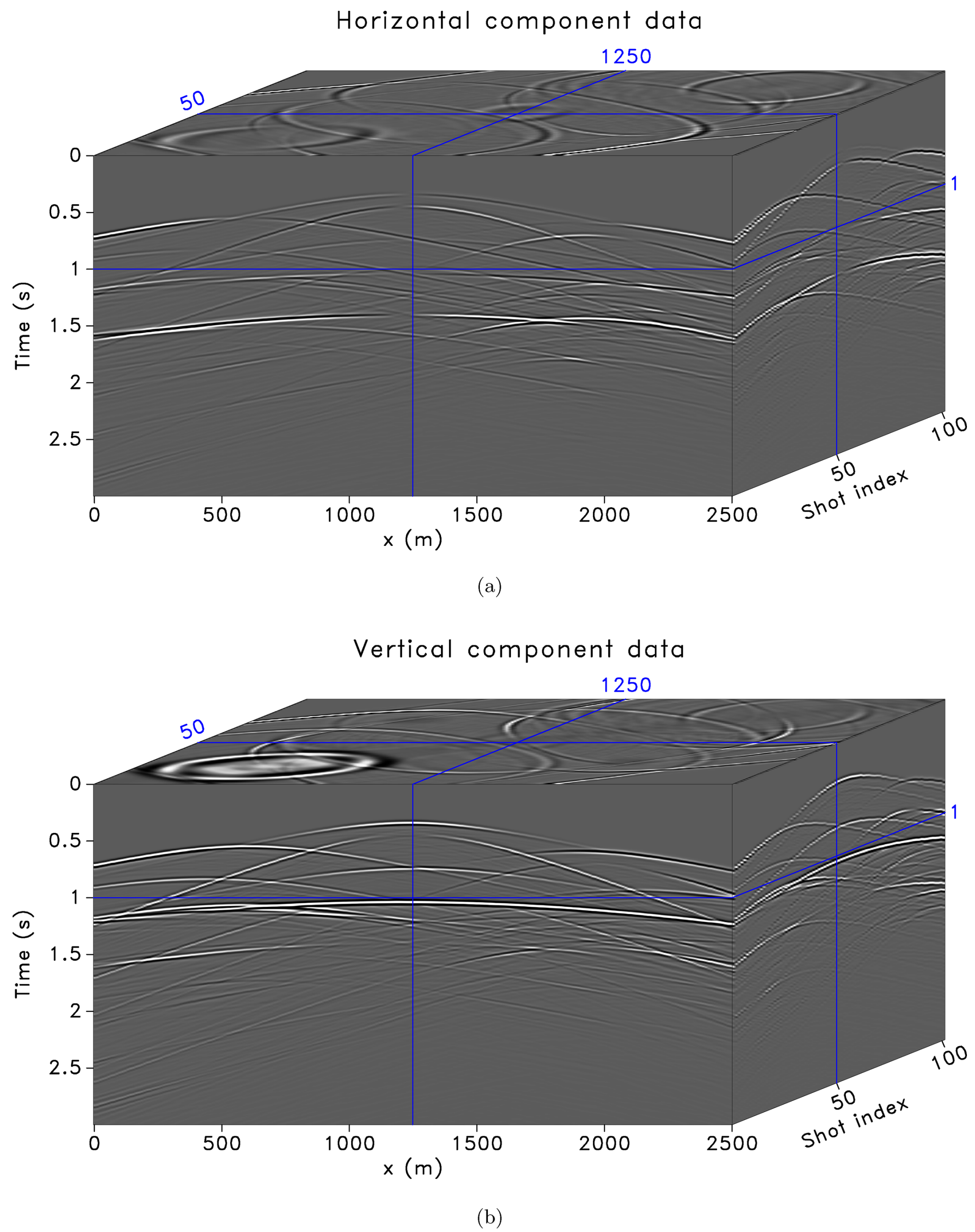

Figure 2. Multicomponent data of the elastic inclusion model. (a) Horizontal particle velocity data. (b) Vertical particle velocity data.

propose a time-domain three-parameter elastic LSRTM algorithm to simultaneously invert for density perturbation, *P*- and *S*-wave velocity perturbation. The latter complements our previous work on elastic LSRTM (Chen & Sacchi 2017). Our three-parameter elastic LSRTM algorithm directly adopts the elastic wave equation without splitting the equation to *P*- and *S*-wave components as in Qu *et al.* (2018). We derive the elastic Born approximation and elastic RTM operators using the continuous adjoint-state method (Lions 1971; Tarantola 1988; Tromp *et al.* 2005; Fichtner *et al.* 2006a,b; Plessix 2006; Fichtner 2010; Chen & Lee 2015). We carefully discretize the two operators to ensure that they pass the dot-product test. The latter allows us to use the conjugate gradient least-squares (CGLS) method to solve the LSM optimization problem. We show that the proposed three-parameter elastic LSRTM algorithm is able to mitigate the crosstalk among density, *P*- and *S*-wave velocity perturbations. Moreover, it improves the convergence and data fitting over the conventional two-parameter elastic LSRTM. Because of computational resource limit, we present numerical examples in 2-D case. However, the proposed method can be extended to 3-D naturally.

Downloaded from https://academic.oup.com/gji/article-abstract/216/1/61/5091812 by University of California, Berkeley/LBL user on 21 June 2019

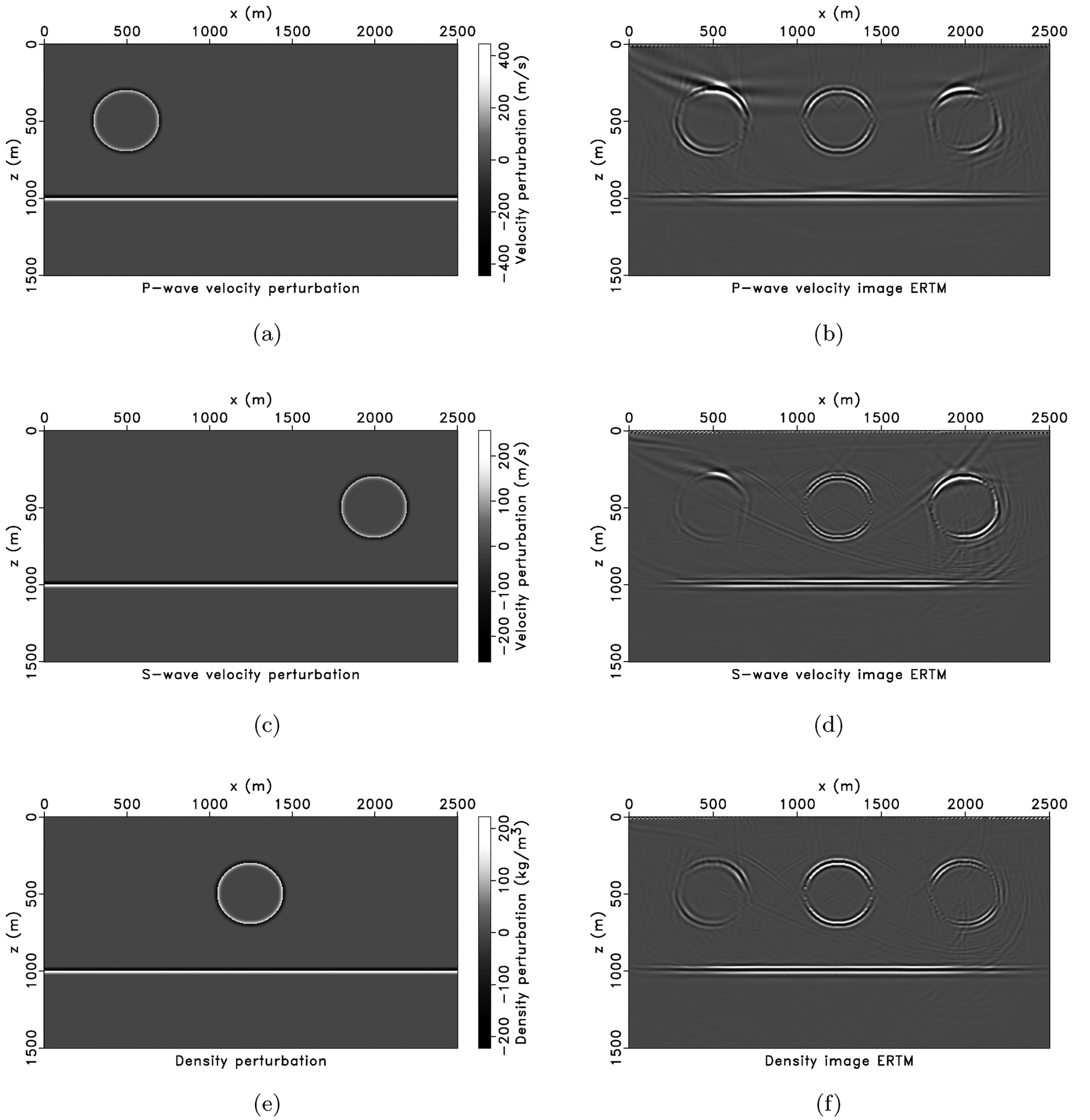

Figure 3. (a) True *P*-wave velocity perturbation. (b) *P*-wave velocity perturbation image estimated via elastic RTM. (c) True *S*-wave velocity perturbation. (d) *S*-wave velocity perturbation image estimated via elastic RTM. (e) True density perturbation. (f) Density perturbation image estimated via elastic RTM.

We have organized this paper as follows. First, we describe the wave equation that we have adopted to simulate elastic wavefields. Then, we introduce the three-parameter elastic Born approximation and the elastic RTM operators. Subsequently, we present the proposed three-parameter elastic LSRTM algorithm. In the last section, we evaluate the performance of the proposed algorithm with numerical examples.

THEORY

Elastic wave equation

The propagation of seismic wave in a heterogeneous, isotropic elastic Earth media is described by the elastic wave equation (Virieux 1986)

Downloaded from https://academic.oup.com/gji/article-abstract/216/1/61/5091812 by University of California, Berkeley/LBL user on 21 June 2019

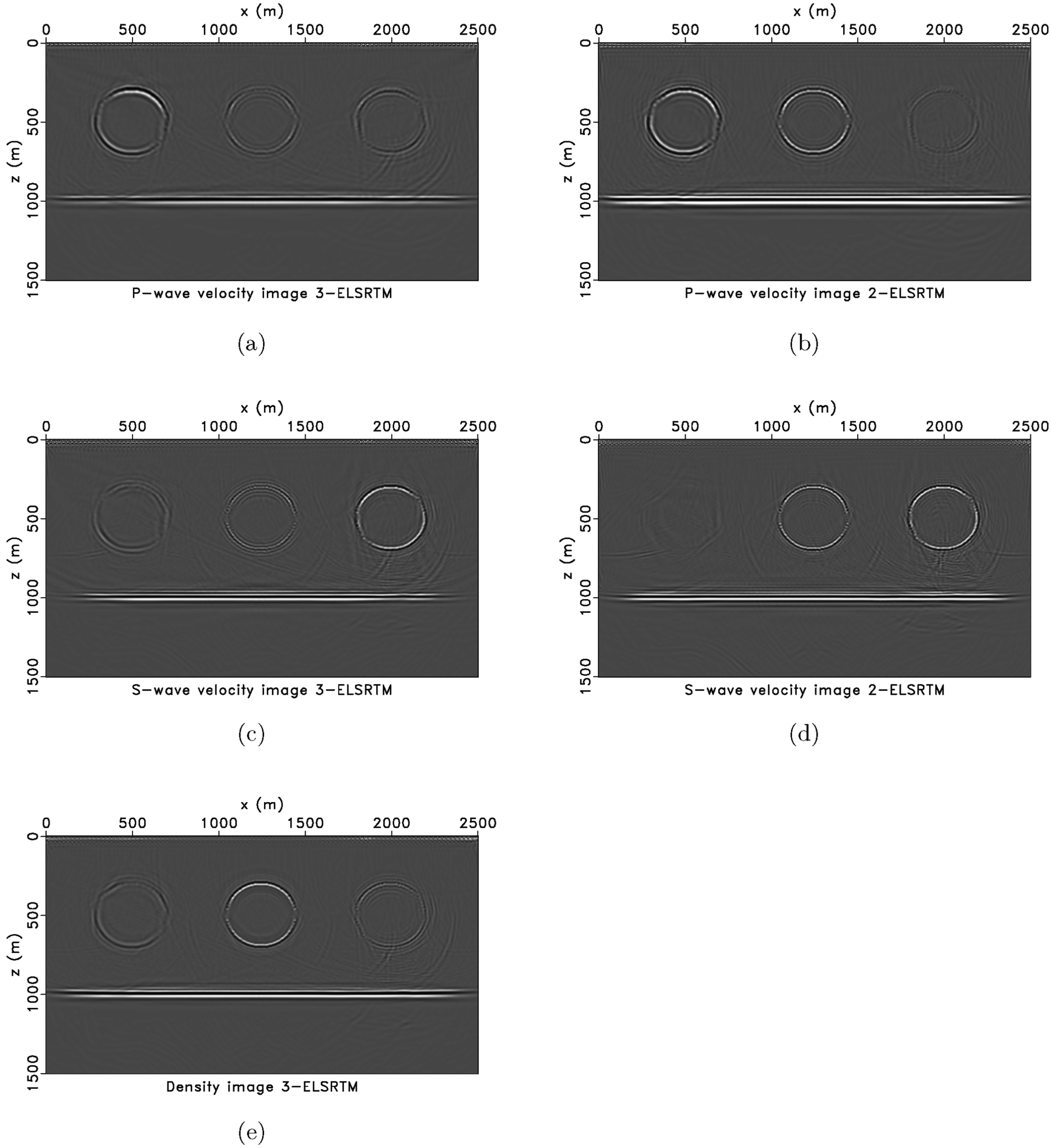

Figure 4. *P*-wave velocity perturbation image estimated via three-parameter elastic LSRTM (a) and two-parameter elastic LSRTM (b). *S*-wave velocity perturbation image estimated via three-parameter elastic LSRTM (c) and two-parameter elastic LSRTM (d). Density perturbation image estimated via three-parameter elastic LSRTM (e).

Downloaded from https://academic.oup.com/gji/article-abstract/216/1/61/5091812 by University of California, Berkeley/LBL user on 21 June 2019

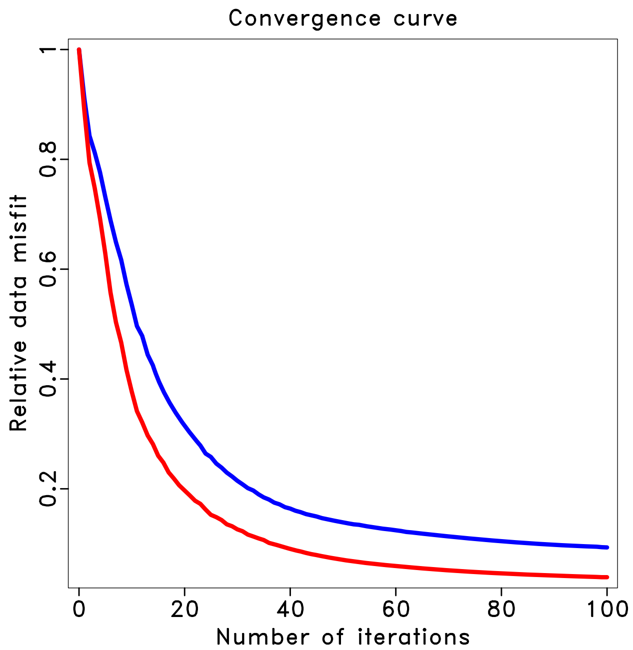

Figure 5. Comparison of the convergence curves of three-parameter elastic LSRTM (red) and two-parameter elastic LSRTM (blue) for elastic inclusion model.

$$
\begin{aligned}
&\rho\frac{\partial v_x}{\partial t}-\left(\frac{\partial\sigma_{xx}}{\partial x}+\frac{\partial\sigma_{xz}}{\partial z}\right)=0,\\
&\rho\frac{\partial v_z}{\partial t}-\left(\frac{\partial\sigma_{xz}}{\partial x}+\frac{\partial\sigma_{zz}}{\partial z}\right)=0,\\
&\frac{\partial\sigma_{xx}}{\partial t}-(\lambda+2\mu)\frac{\partial v_x}{\partial x}-\lambda\frac{\partial v_z}{\partial z}=f_{xx},\\
&\frac{\partial\sigma_{zz}}{\partial t}-(\lambda+2\mu)\frac{\partial v_z}{\partial z}-\lambda\frac{\partial v_x}{\partial x}=f_{zz},\\
&\frac{\partial\sigma_{xz}}{\partial t}-\mu\left(\frac{\partial v_x}{\partial z}+\frac{\partial v_z}{\partial x}\right)=0,
\end{aligned}
\tag{1}
$$

where v_x and v_z are the horizontal and vertical particle velocity fields, σ_{xx}, σ_{xz} and σ_{zz} are the stress fields, ρ is the density, λ and μ are the Lamé parameters, and f_{xx} and f_{zz} are the explosive source terms. In the wave equation, we dropped the dependence on spatial and temporal coordinates $\mathbf{x}$ and t of our variables to make the notations concise but we understand that $v_x = v_x(\mathbf{x}, t)$, $\lambda = \lambda(\mathbf{x})$, etc. The elastic wave equation can be written in abstract functional form as follows:

$$\mathbf{S}(\bar{\mathbf{m}})\mathbf{u}=\mathbf{f}, \tag{2}$$

where $\bar{\mathbf{m}} = (\rho, \lambda, \mu)^T$ denotes the model parameter vector, $\mathbf{S}$ is the wave equation operator, $\mathbf{u} = (v_x, v_z, \sigma_{xx}, \sigma_{zz}, \sigma_{xz})^T$ is the wavefield vector and $\mathbf{f} = (0, 0, f_{xx}, f_{zz}, 0)^T$ is the source vector. The seismic data are observed by receivers

$$\mathbf{d}=\mathbf{R}\mathbf{u}, \tag{3}$$

where $\mathbf{d} = (d_{v_x}, d_{v_z}, 0, 0, 0)^T$ is the seismic data vector and $\mathbf{R}$ is the sampling operator.

Elastic Born approximation

Seismic migration techniques in oil and gas exploration rely on the concept of the Born approximation. A perturbation around the known background model parameters

$$\rho\rightarrow\rho+\delta\rho, \tag{4a}$$

$$\lambda\rightarrow\lambda+\delta\lambda, \tag{4b}$$

$$\mu\rightarrow\mu+\delta\mu, \tag{4c}$$

leads to a perturbation of the wavefields

$$v_x\rightarrow v_x+\delta v_x, \tag{4d}$$

$$v_z\rightarrow v_z+\delta v_z, \tag{4e}$$

$$\sigma_{xx}\rightarrow\sigma_{xx}+\delta\sigma_{xx}, \tag{4f}$$

$$\sigma_{zz}\rightarrow\sigma_{zz}+\delta\sigma_{zz}, \tag{4g}$$

$$\sigma_{xz}\rightarrow\sigma_{xz}+\delta\sigma_{xz}. \tag{4h}$$

Inserting eq. (4) into eq. (1), subtracting eq. (1) and dropping second- and higher-order terms leads to the Born approximation for the first-order velocity stress elastic wave equation system (Chen & Sacchi 2017)

$$
\begin{aligned}
&\rho\frac{\partial\delta v_x}{\partial t}-\left(\frac{\partial\delta\sigma_{xx}}{\partial x}+\frac{\partial\delta\sigma_{xz}}{\partial z}\right)=-\delta\rho\dot{v}_x,\\
&\rho\frac{\partial\delta v_z}{\partial t}-\left(\frac{\partial\delta\sigma_{xz}}{\partial x}+\frac{\partial\delta\sigma_{zz}}{\partial z}\right)=-\delta\rho\dot{v}_z,\\
&\frac{\partial\delta\sigma_{xx}}{\partial t}-(\lambda+2\mu)\frac{\partial\delta v_x}{\partial x}-\lambda\frac{\partial\delta v_z}{\partial z}=(\delta\lambda+\delta\mu)\frac{\dot{\sigma}_{xx}+\dot{\sigma}_{zz}}{2(\lambda+\mu)}\\
&\qquad+\delta\mu\frac{\dot{\sigma}_{xx}-\dot{\sigma}_{zz}}{2\mu},\\
&\frac{\partial\delta\sigma_{zz}}{\partial t}-(\lambda+2\mu)\frac{\partial\delta v_z}{\partial z}-\lambda\frac{\partial\delta v_x}{\partial x}=(\delta\lambda+\delta\mu)\frac{\dot{\sigma}_{xx}+\dot{\sigma}_{zz}}{2(\lambda+\mu)}\\
&\qquad-\delta\mu\frac{\dot{\sigma}_{xx}-\dot{\sigma}_{zz}}{2\mu},\\
&\frac{\partial\delta\sigma_{xz}}{\partial t}-\mu\left(\frac{\partial\delta v_x}{\partial z}+\frac{\partial\delta v_z}{\partial x}\right)=\delta\mu\frac{\dot{\sigma}_{xz}}{\mu},
\end{aligned}
\tag{5}
$$

where $\mathbf{u} = (v_x, v_z, \sigma_{xx}, \sigma_{zz}, \sigma_{xz})^T$ is the incident wavefield or called source-side wavefield in the background model $\bar{\mathbf{m}} = (\rho, \lambda, \mu)^T$, $\delta\mathbf{u} = (\delta v_x, \delta v_z, \delta\sigma_{xx}, \delta\sigma_{zz}, \delta\sigma_{xz})^T$ is the scattered wavefield due to model perturbation $\delta\bar{\mathbf{m}} = (\delta\rho, \delta\lambda, \delta\mu)^T$ and over-dot means the time derivative. We parametrize our three-parameter elastic LSRTM in terms of density, *P*- and *S*-wave velocity perturbations. The different model parameter perturbations obey the following expressions:

$$
\begin{pmatrix}\delta\rho\\ \delta\lambda\\ \delta\mu\end{pmatrix}=\begin{pmatrix}1 & 0 & 0\\ V_p^2-2V_s^2 & 2\rho V_p & -4\rho V_s\\ V_s^2 & 0 & 2\rho V_s\end{pmatrix}\begin{pmatrix}\delta\varrho\\ \delta V_p\\ \delta V_s\end{pmatrix},
\tag{6}
$$

where $V_p = \sqrt{(\lambda+2\mu)/\rho}$ and $V_s = \sqrt{\mu/\rho}$ are background *P*- and *S*-wave velocities, δV_p and δV_s are *P*- and *S*-wave velocity perturbations.

Downloaded from https://academic.oup.com/gji/article-abstract/216/1/61/5091812 by University of California, Berkeley/LBL user on 21 June 2019

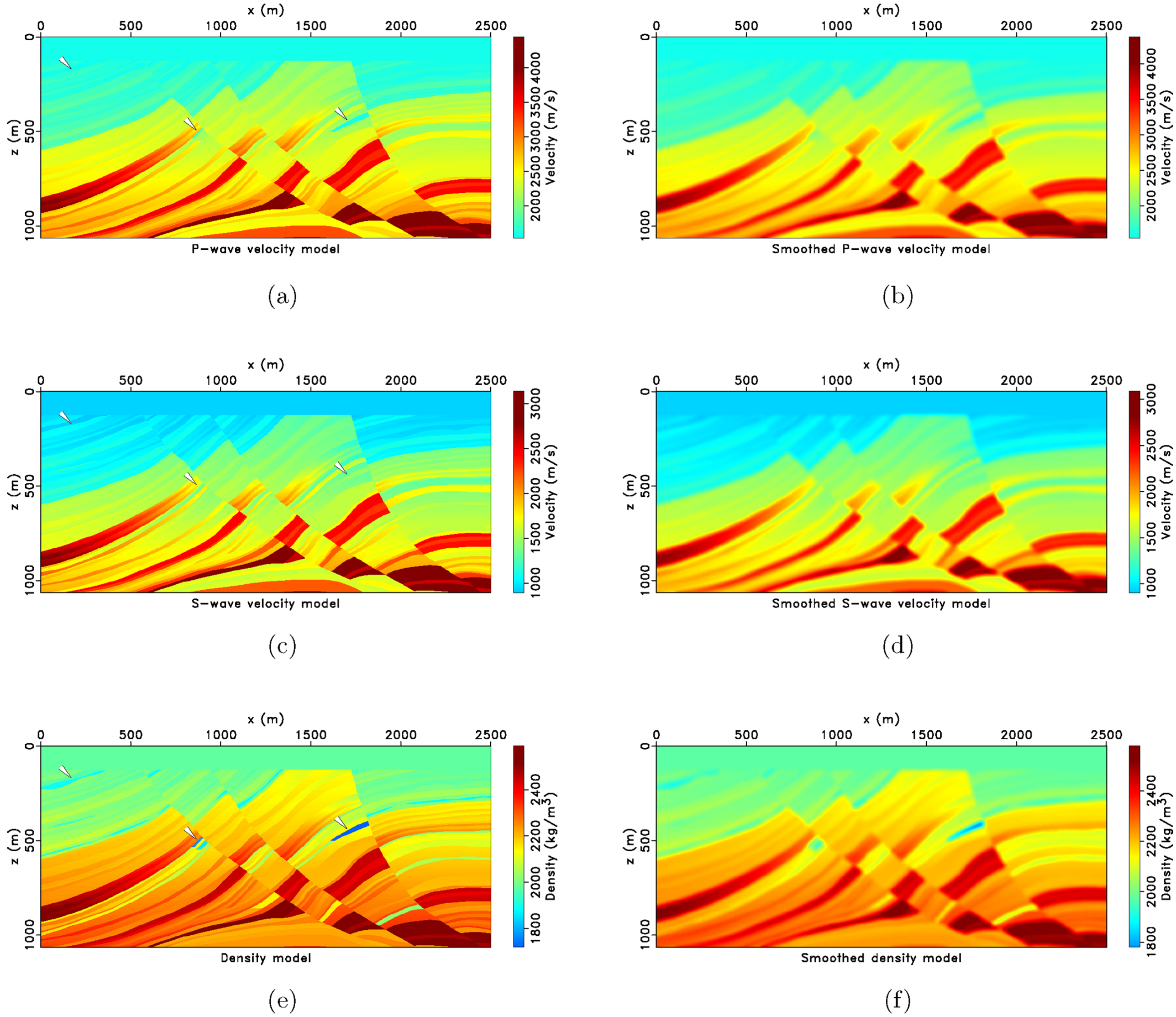

Figure 6. Elastic Marmousi2 model. (a) *P*-wave velocity model. (b) Smoothed *P*-wave velocity model. (c) *S*-wave velocity model. (d) Smoothed *S*-wave velocity model. (e) Density model. (f) Smoothed density model.

We can also express the above expressions in abstract functional form. The model perturbation $\bar{\mathbf{m}} \to \bar{\mathbf{m}} + \delta\bar{\mathbf{m}}$ leads to a perturbation in wave equation (2)

$$(\mathbf{S} + \delta\mathbf{S})(\mathbf{u} + \delta\mathbf{u}) = \mathbf{f}, \tag{7}$$

where $\delta\mathbf{S}$ is the wave equation operator perturbation, $\delta\mathbf{u}$ is the wavefield perturbation, $\mathbf{S}$ is the wave equation operator in background model and $\mathbf{u}$ is the wavefield in background model. Using wave equation $\mathbf{S}\mathbf{u} = \mathbf{f}$ and neglecting second-order term, eq. (7) can be simplified as

$$\mathbf{S}\delta\mathbf{u} = -\delta\mathbf{S}\mathbf{u}. \tag{8}$$

The perturbed seismic data can be expressed as

$$\delta\mathbf{d} = \mathbf{R}\delta\mathbf{u} = -\mathbf{R}\mathbf{S}^{-1}\delta\mathbf{S}\mathbf{u} = -\mathbf{R}\mathbf{S}^{-1}\frac{\partial\mathbf{S}}{\partial\bar{\mathbf{m}}}\mathbf{u}\delta\bar{\mathbf{m}}, \tag{9}$$

where $\mathbf{R}$ is the sampling operator, $\mathbf{S}^{-1}$ is the inverse of wave equation operator and the linear operator $\partial\mathbf{S}/\partial\bar{\mathbf{m}}$ denotes the diffraction pattern of density and Lamé parameters (Operto *et al.* 2013; Pageot *et al.* 2013). The vector $\delta\bar{\mathbf{m}} = (\delta\rho, \delta\lambda, \delta\mu)^T$ denotes density and Lamé parameters perturbations. The parameter perturbations are connected via

$$\delta\bar{\mathbf{m}} = \mathbf{T}\delta\mathbf{m}, \tag{10}$$

where $\mathbf{T}$ denotes the transformation matrix in eq. (6), and $\delta\mathbf{m} = (\delta\varrho, \delta V_\mathrm{p}, \delta V_\mathrm{s})^T$. The elastic Born approximation can be expressed in abstract form as

$$\delta\mathbf{d} = \mathbf{L}\delta\mathbf{m} = -\mathbf{R}\mathbf{S}^{-1}\frac{\partial\mathbf{S}}{\partial\bar{\mathbf{m}}}\mathbf{u}\mathbf{T}\delta\mathbf{m}, \tag{11}$$

where operator $\mathbf{L}$ indicates the elastic Born approximation operator.

Elastic reverse time migration

Seismic migration estimates subsurface structural image using the seismic data recorded on the surface of the Earth. Migration can be

Downloaded from https://academic.oup.com/gji/article-abstract/216/1/61/5091812 by University of California, Berkeley/LBL user on 21 June 2019

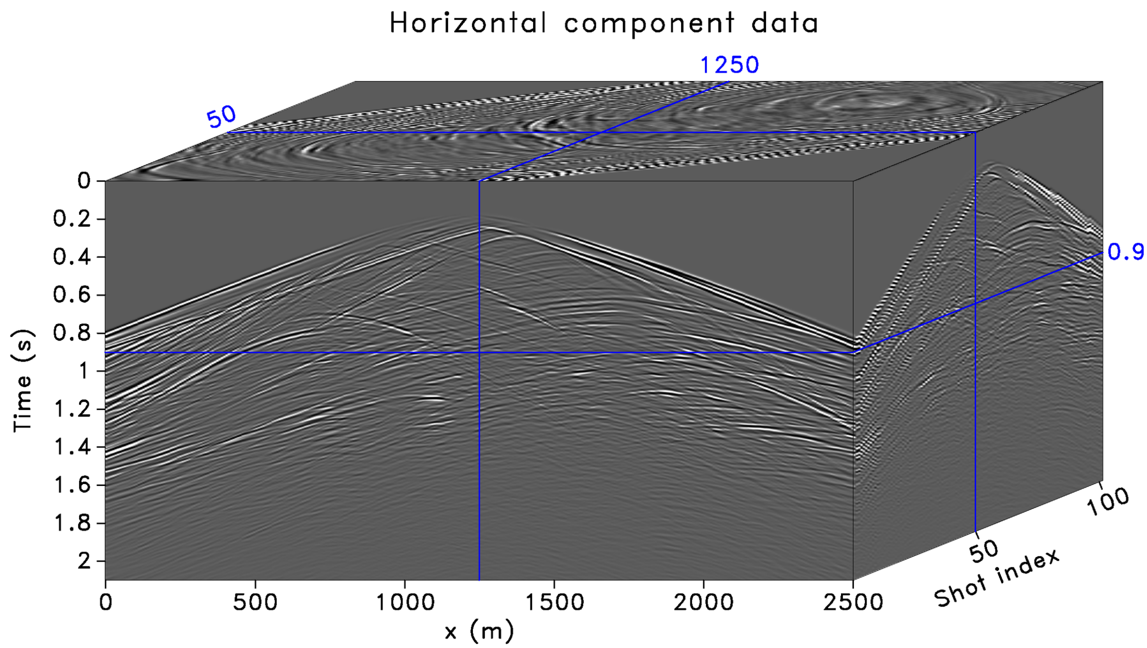

(a)

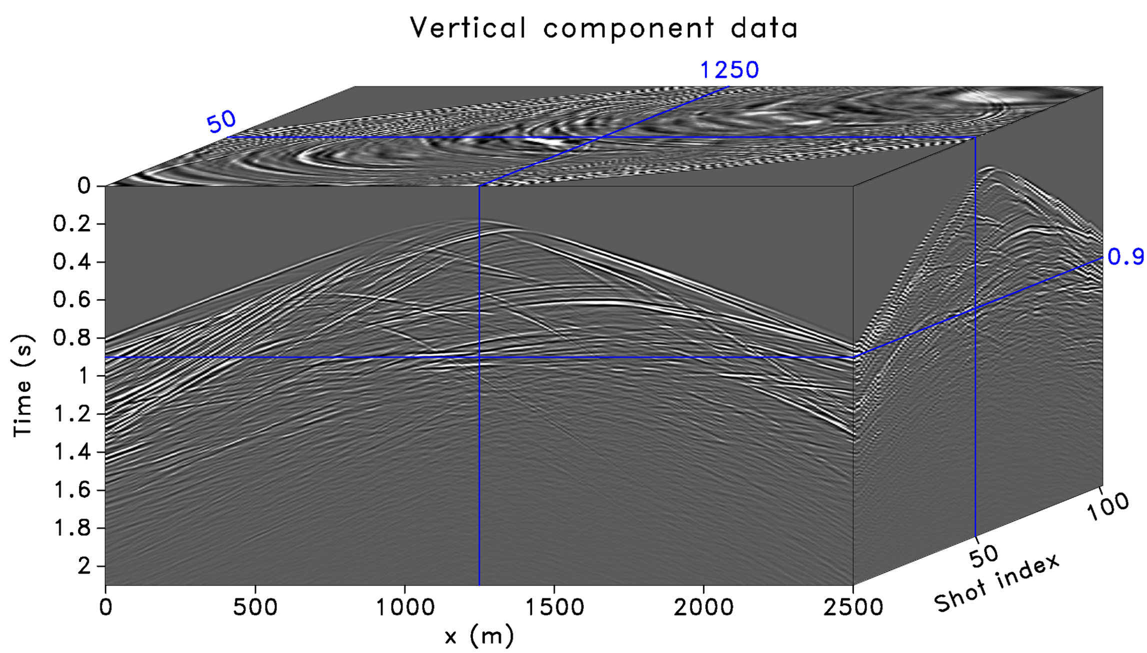

(b)

Figure 7. Multicomponent data of the elastic Marmousi2 model. (a) Horizontal particle velocity data. (b) Vertical particle velocity data.

regarded as the adjoint of the Born approximation operator

$$\delta \mathbf{m}^* = \mathbf{L}^\dagger \delta \mathbf{d} = -\mathbf{T}^\dagger \left(\frac{\partial \mathbf{S}}{\partial \bar{\mathbf{m}}}\mathbf{u}\right)^\dagger \left(\mathbf{S}^{-1}\right)^\dagger \mathbf{R}^\dagger \delta \mathbf{d}$$
$$= -\mathbf{T}^\dagger \left(\frac{\partial \mathbf{S}}{\partial \bar{\mathbf{m}}}\mathbf{u}\right)^\dagger \left(\mathbf{S}^\dagger\right)^{-1} \mathbf{R}^\dagger \delta \mathbf{d}, \quad (12)$$

where † indicates the adjoint of an operator, $\mathbf{L}^\dagger$ is the elastic RTM operator and $\delta \mathbf{m}^*$ is the migrated elastic images ($\delta \mathbf{m}^* = (\delta \varrho^*, \delta V_p^*, \delta V_s^*)^T$). We introduce the adjoint-state variable $\mathbf{p} = (\mathbf{S}^\dagger)^{-1}\mathbf{R}^\dagger \delta \mathbf{d}$. The latter satisfies the adjoint-state equation corresponding to the state equation (2)

$$\mathbf{S}^\dagger \mathbf{p} = \mathbf{R}^\dagger \delta \mathbf{d}, \quad (13)$$

Downloaded from https://academic.oup.com/gji/article-abstract/216/1/61/5091812 by University of California, Berkeley/LBL user on 21 June 2019

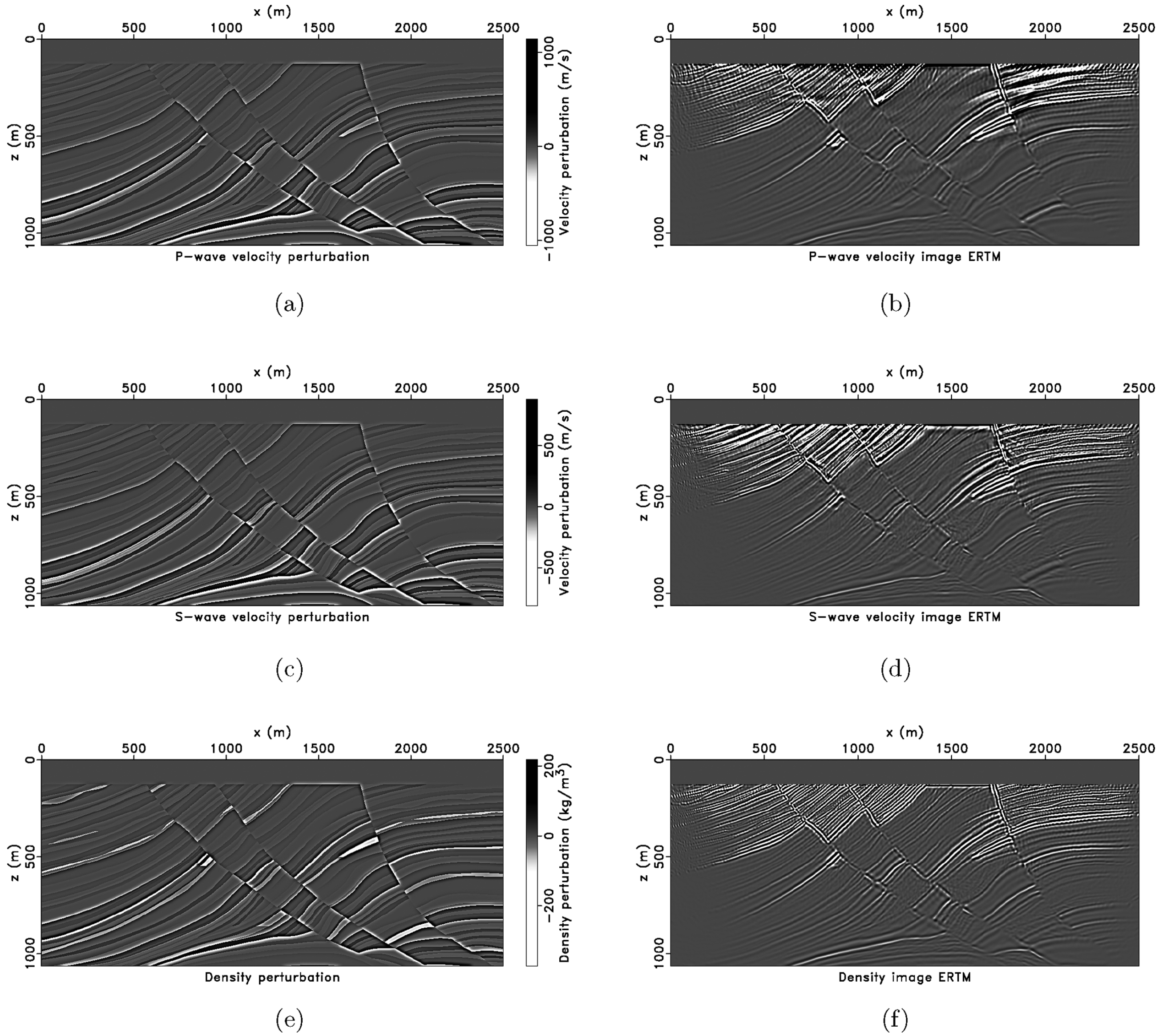

Figure 8. (a) True *P*-wave velocity perturbation. (b) *P*-wave velocity perturbation image estimated via elastic RTM. (c) True *S*-wave velocity perturbation. (d) *S*-wave velocity perturbation image estimated via elastic RTM. (e) True density perturbation. (f) Density perturbation image estimated via elastic RTM.

where $\mathbf{S}^{\dagger}$ is the adjoint wave equation operator and $\mathbf{R}^{\dagger}\delta\mathbf{d}$ is the adjoint source. The migrated elastic images can be simplified as

$$\delta\mathbf{m}^{*} = -\mathbf{T}^{\dagger}\left(\frac{\partial\mathbf{S}}{\partial\bar{\mathbf{m}}}\mathbf{u}\right)^{\dagger}\mathbf{p} = -\mathbf{T}^{\dagger}\delta\bar{\mathbf{m}}^{*}, \tag{14}$$

where $\mathbf{T}^{\dagger}$ is the adjoint of the transformation matrix in eq. (6) and $\delta\bar{\mathbf{m}}^{*} = (\delta\rho^{*}, \delta\lambda^{*}, \delta\mu^{*})^{T}$. The image expression in eq. (14) is very similar to Claerbout's cross-correlation imaging condition (Claerbout 1985) but has an additional operator applied on the wavefield.

The adjoint-state equation corresponding to the first-order velocity-stress elastic wave equation (1) can be derived

$$\begin{aligned}
&-\rho\frac{\partial \upsilon_x}{\partial t} + \left(\frac{\partial \tau_{xx}}{\partial x} + \frac{\partial \tau_{xz}}{\partial z}\right) = \delta d_{\upsilon_x},\\
&-\rho\frac{\partial \upsilon_z}{\partial t} + \left(\frac{\partial \tau_{xz}}{\partial x} + \frac{\partial \tau_{zz}}{\partial z}\right) = \delta d_{\upsilon_z},\\
&-\frac{\partial \tau_{xx}}{\partial t} + (\lambda + 2\mu)\frac{\partial \upsilon_x}{\partial x} + \lambda\frac{\partial \upsilon_z}{\partial z} = 0,\\
&-\frac{\partial \tau_{zz}}{\partial t} + (\lambda + 2\mu)\frac{\partial \upsilon_z}{\partial z} + \lambda\frac{\partial \upsilon_x}{\partial x} = 0,\\
&-\frac{\partial \tau_{xz}}{\partial t} + \mu\left(\frac{\partial \upsilon_x}{\partial z} + \frac{\partial \upsilon_z}{\partial x}\right) = 0,
\end{aligned} \tag{15}$$

Downloaded from https://academic.oup.com/gji/article-abstract/216/1/61/5091812 by University of California, Berkeley/LBL user on 21 June 2019

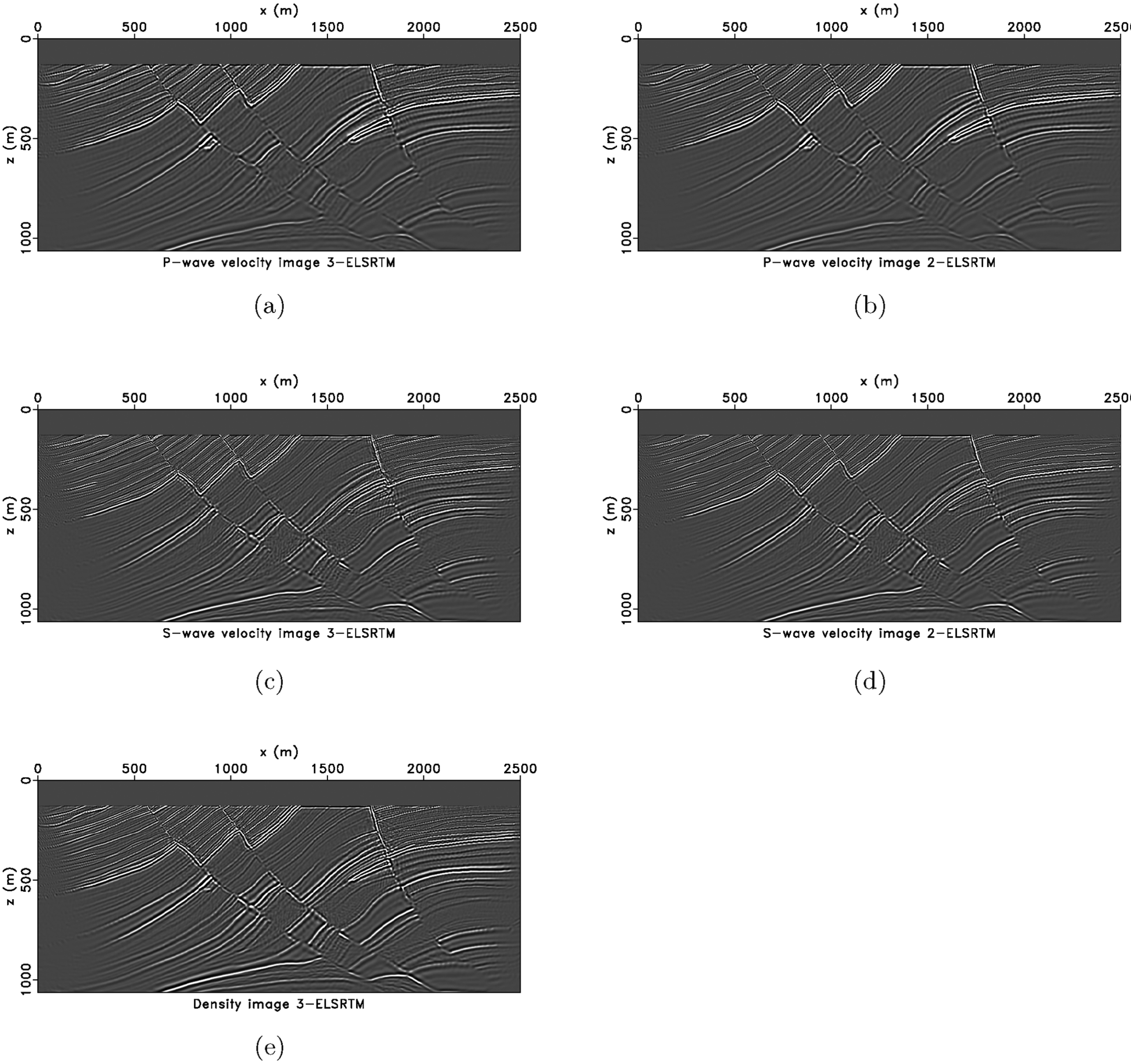

Figure 9. *P*-wave velocity perturbation image estimated via three-parameter elastic LSRTM (a) and two-parameter elastic LSRTM (b). *S*-wave velocity perturbation image estimated via three-parameter elastic LSRTM (c) and two-parameter elastic LSRTM (d). Density perturbation image estimated via three-parameter elastic LSRTM (e).

where $\mathbf{p} = (\upsilon_x, \upsilon_z, \tau_{xx}, \tau_{zz}, \tau_{xz})^T$ is the adjoint-state wavefield and $\delta\mathbf{d} = (\delta d_{v_x}, \delta d_{v_z}, 0, 0, 0)^T$ is the data residual. The migrated density and Lamé parameter images can be written as

$$\delta\rho^* = -\int (\dot{v}_x \upsilon_x + \dot{v}_z \upsilon_z)\mathrm{d}t,$$

$$\delta\lambda^* = \int \frac{(\dot{\sigma}_{xx} + \dot{\sigma}_{zz})(\tau_{xx} + \tau_{zz})}{4(\lambda + \mu)^2}\mathrm{d}t,$$

$$\delta\mu^* = \int \left[\frac{\dot{\sigma}_{xz}\tau_{xz}}{\mu^2} + \frac{(\dot{\sigma}_{xx} + \dot{\sigma}_{zz})(\tau_{xx} + \tau_{zz})}{4(\lambda + \mu)^2} + \frac{(\dot{\sigma}_{xx} - \dot{\sigma}_{zz})(\tau_{xx} - \tau_{zz})}{4\mu^2}\right]\mathrm{d}t. \quad (16)$$

The density and Lamé parameter perturbations can be transformed to density and wave velocity perturbations

$$\begin{pmatrix} \delta\varrho^* \\ \delta V_\mathrm{p}^* \\ \delta V_\mathrm{s}^* \end{pmatrix} = \begin{pmatrix} 1 & V_\mathrm{p}^2 - 2V_\mathrm{s}^2 & V_\mathrm{s}^2 \\ 0 & 2\rho V_\mathrm{p} & 0 \\ 0 & -4\rho V_\mathrm{s} & 2\rho V_\mathrm{s} \end{pmatrix} \begin{pmatrix} \delta\rho^* \\ \delta\lambda^* \\ \delta\mu^* \end{pmatrix}. \quad (17)$$

Three-parameter elastic least-squares reverse time migration

To improve the spatial resolution of images and reduce the crosstalk and artefacts in the images, we formulate the three-parameter elastic

Downloaded from https://academic.oup.com/gji/article-abstract/216/1/61/5091812 by University of California, Berkeley/LBL user on 21 June 2019

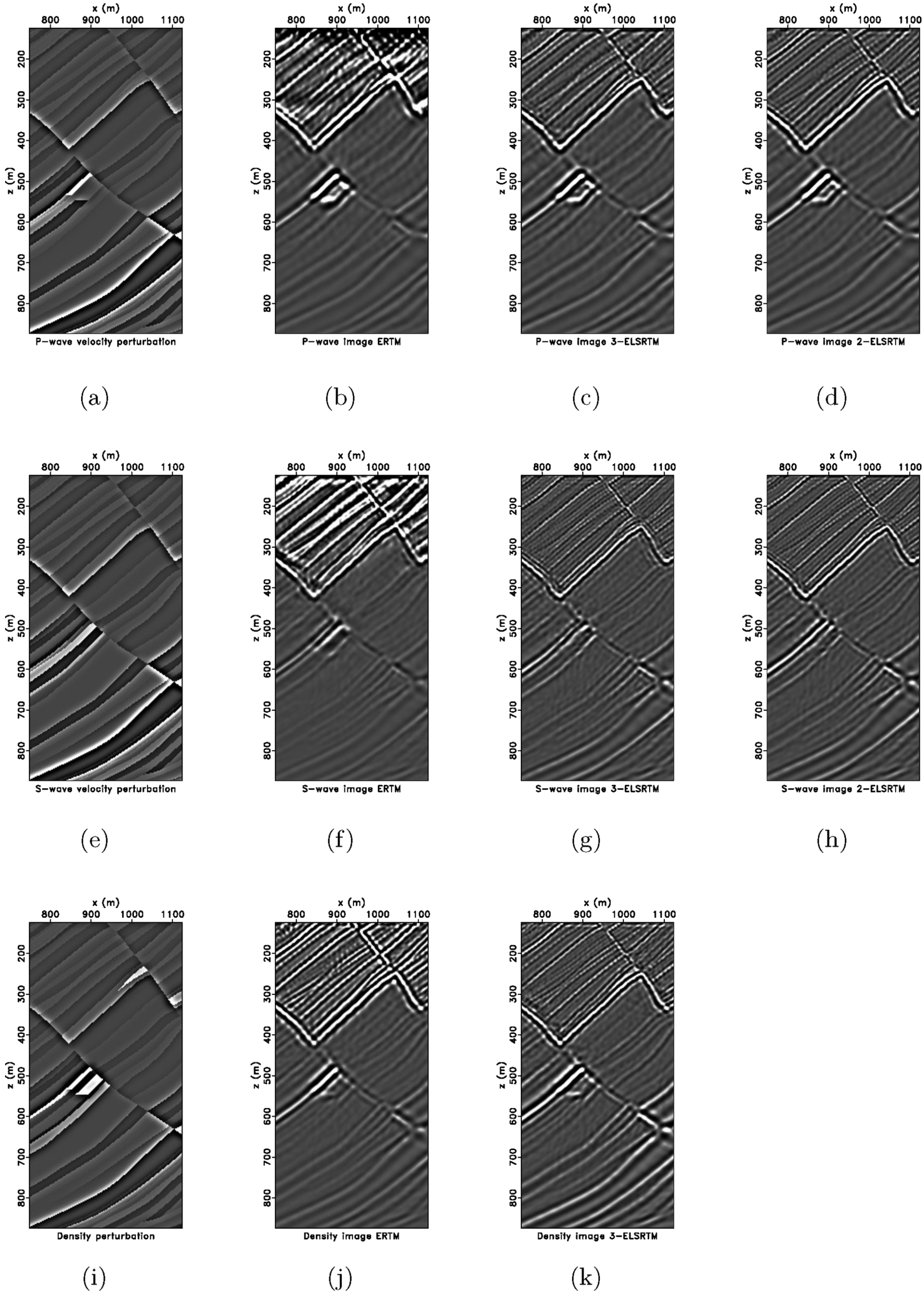

Figure 10. Comparison of images in the range 750 m $< x <$ 1125 m and 125 m $< z <$ 875 m. *P*-wave velocity perturbation: (a) true model, (b) elastic RTM, (c) three-parameter elastic LSRTM, (d) two-parameter elastic LSRTM. *S*-wave velocity perturbation: (e) true model, (f) elastic RTM, (g) three-parameter elastic LSRTM, (h) two-parameter elastic LSRTM. Density perturbation: (i) true model, (j) elastic RTM, (k) three-parameter elastic LSRTM.

Downloaded from https://academic.oup.com/gji/article-abstract/216/1/61/5091812 by University of California, Berkeley/LBL user on 21 June 2019

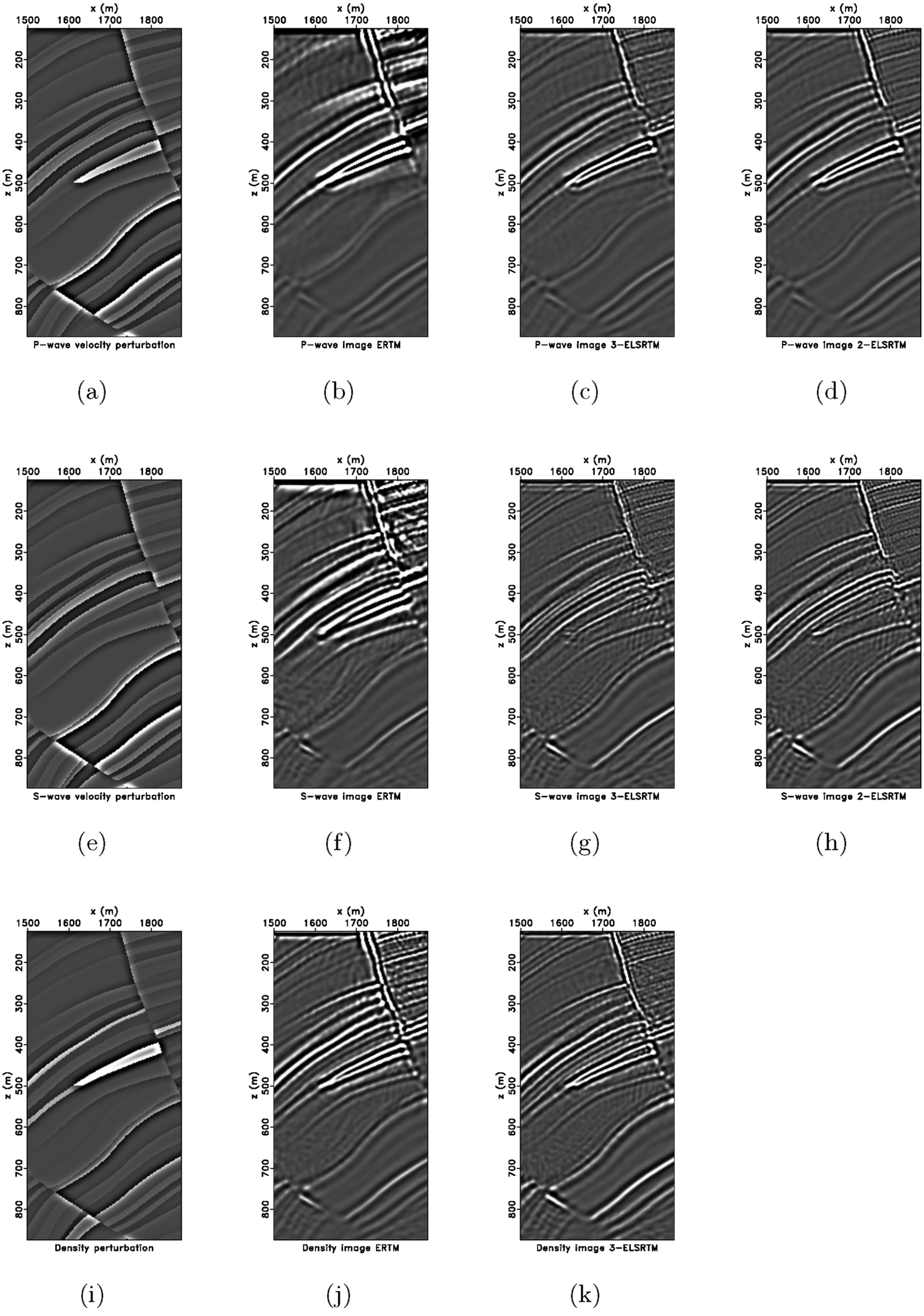

Figure 11. Comparison of images in the range 1500 m $< x <$ 1875 m and 125 m $< z <$ 875 m. *P*-wave velocity perturbation: (a) true model, (b) elastic RTM, (c) three-parameter elastic LSRTM, (d) two-parameter elastic LSRTM. *S*-wave velocity perturbation: (e) true model, (f) elastic RTM, (g) three-parameter elastic LSRTM, (h) two-parameter elastic LSRTM. Density perturbation: (i) true model, (j) elastic RTM, (k) three-parameter elastic LSRTM.

Downloaded from https://academic.oup.com/gji/article-abstract/216/1/61/5091812 by University of California, Berkeley/LBL user on 21 June 2019

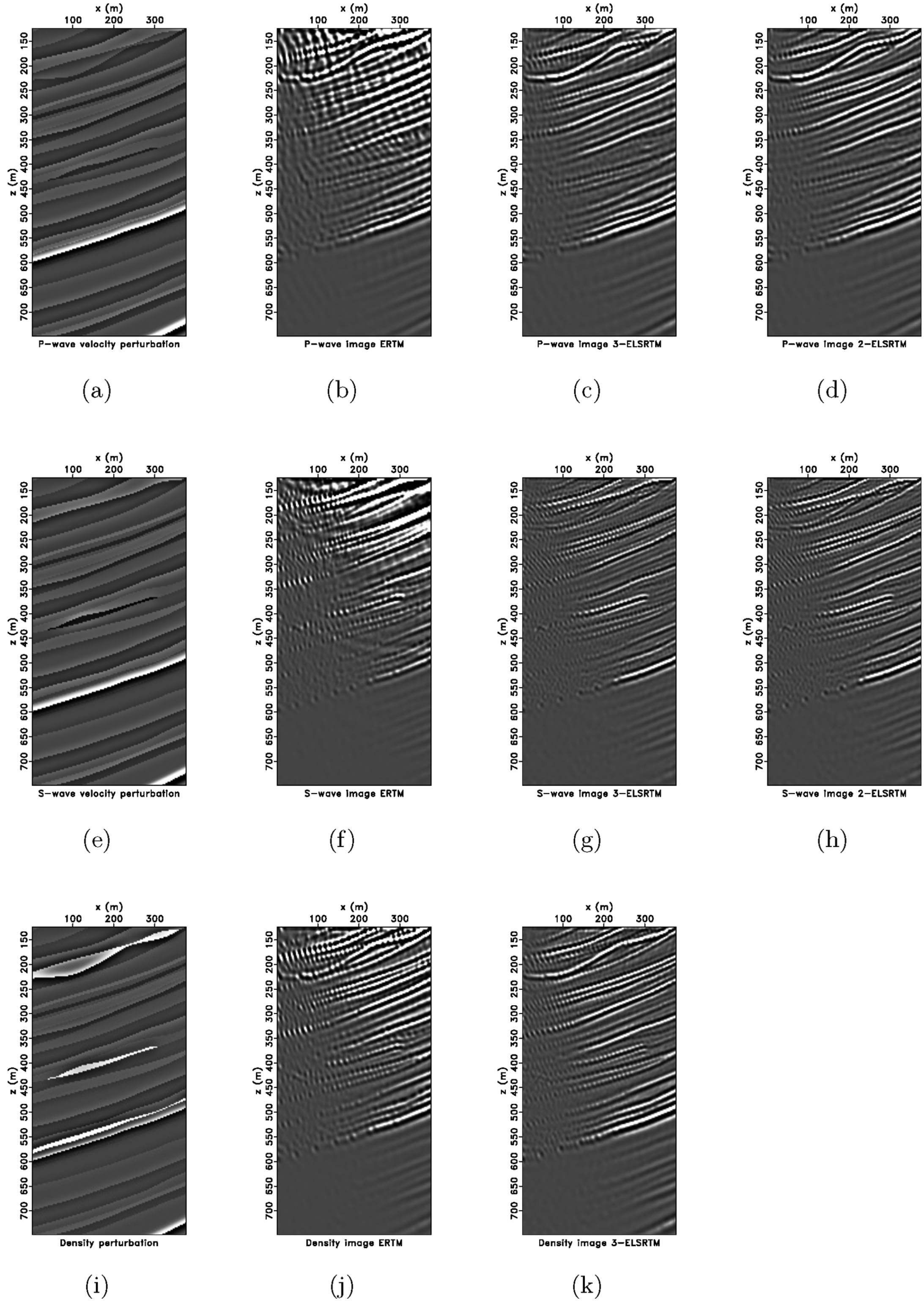

Figure 12. Comparison of images in the range 0 m < x < 375 m and 125 m < z < 750 m. *P*-wave velocity perturbation: (a) true model, (b) elastic RTM, (c) three-parameter elastic LSRTM, (d) two-parameter elastic LSRTM. *S*-wave velocity perturbation: (e) true model, (f) elastic RTM, (g) three-parameter elastic LSRTM, (h) two-parameter elastic LSRTM. Density perturbation: (i) true model, (j) elastic RTM, (k) three-parameter elastic LSRTM.

Downloaded from https://academic.oup.com/gji/article-abstract/216/1/61/5091812 by University of California, Berkeley/LBL user on 21 June 2019

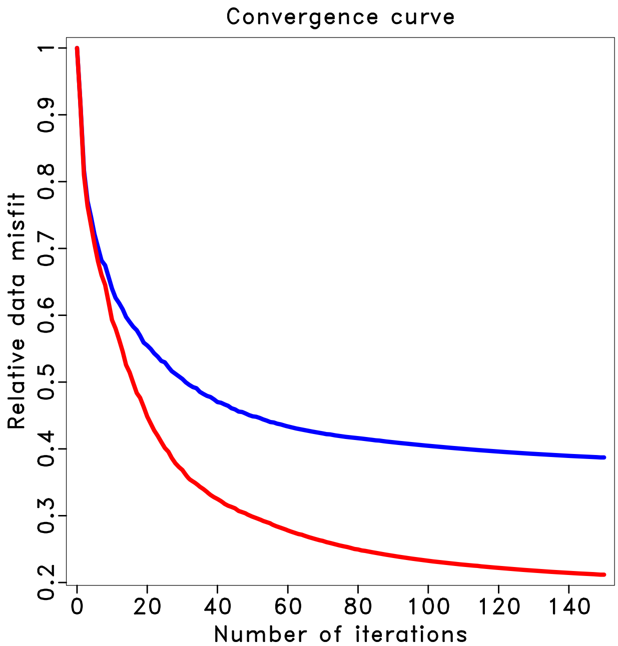

Figure 13. Comparison of the convergence curves of three-parameter elastic LSRTM (red) and two-parameter elastic LSRTM (blue) for elastic Marmousi2 model.

LSRTM as a least-squares inversion problem

$$J = \frac{1}{2}\sum_{i=1}^{N_s} \|\mathbf{L}_i \delta\mathbf{m} - \delta\mathbf{d}_i\|_2^2, \tag{18}$$

where $\mathbf{L}_i$ is the elastic Born approximation operator for the ith shot, $\delta\mathbf{d}_i$ is the ith shot gather, $\delta\mathbf{m} = (\delta\varrho, \delta V_p, \delta V_s)^T$ denotes elastic images, N_s indicates the number of shots and $\|\cdot\|_2$ indicates the ℓ_2 norm of vector. It is important to mention that we carefully discretize the elastic Born and RTM operators ($\mathbf{L}_i$ and $\mathbf{L}_i^\dagger$) to assure they pass the dot-product test (Claerbout 1992; Chen & Sacchi 2017). We adopt the CGLS algorithm (Hestenes & Stiefel 1952; Paige & Saunders 1982; Bjorck 1996) to solve eq. (18). The latter only requires two operators $\mathbf{L}_i$ and $\mathbf{L}_i^\dagger$ that are applied 'on the fly' to vectors.

NUMERICAL EXAMPLES

Our code was written in C language and parallelized with Message Passing Interface over shots. The communication between different threads happens when the gradients are collected or distributed in each elastic LSRTM iteration. Our forward-modelling engine adopts a time-domain staggered-grid finite-difference (FD) scheme (Virieux 1986) to discretize the elastic wave equation and the unsplit convolutional perfectly matched layer boundary (Komatitsch & Martin 2007) to absorb the artificial reflections from computational boundaries. In our code, the spatial FD order is selectable. The code automatically computes the FD coefficients from the user-specified FD order (Liu & Sen 2009). In our elastic RTM code ($\mathbf{L}^\dagger$), we use the source-wavefield reconstruction method (Gauthier *et al.* 1986; Dussaud *et al.* 2008) to avoid saving the entire forward source-side wavefield. Our elastic Born ($\mathbf{L}$) and RTM ($\mathbf{L}^\dagger$) codes pass the dot-product test (Claerbout 1992). We present two numerical examples to test the proposed algorithm. We compare the results of the proposed three-parameter elastic LSRTM and the results of two-parameter elastic LSRTM (Chen & Sacchi 2017). The two-parameter elastic LSRTM takes the heterogeneous background density, P- and S-wave velocity models as input models. We emphasize that our synthetic multicomponent data are the solution of the time-domain elastic wave equation (1). We do NOT use the linearized Born modelling to generate data. The data contain multiples that are not honoured by the linearized Born modelling.

Elastic inclusion model

Figs 1(a), (c) and (e) show the true *P*- and *S*-wave velocity and density models. This model may not be realistic. However, it is useful to demonstrate the multiparameter crosstalk in the elastic imaging. The model has 501 × 301 grid points with grid interval of 5 m. There are 101 shots located along the surface of the model with an interval of 25 m. There are 501 receivers located along the surface of the model with an interval of 5 m. We use a Ricker wavelet with central frequency 20 Hz as the source wavelet. The observed data (Fig. 2) are simulated using our time-domain elastic FD code. The data contain full-wave modes except for direct waves. Figs 1(b), (d) and (f) are the migration *P*- and *S*-wave velocity and density models. The migration models are obtained by convolving the true models with a 2-D Gaussian filter of 50 m width. Figs 3(a), (c) and (e) show the true *P*- and *S*-wave velocity and density perturbations.

The elastic RTM generates images with strong multiparameter crosstalk (Figs 3b, d and f). The elastic RTM images are obtained by kernels in eq. (16). Results, in this case, cannot be interpreted properly. Moreover, there are high-amplitude low-frequency RTM artefacts in the images even after applying a Laplacian filtering. We adopted a number of 80 iterations for the two-parameter elastic LSRTM. The relative data misfit reduces to 10 per cent. Our results show that the method reduced the crosstalk between the *P*- and *S*-wave velocity perturbation images (Figs 4b and d). However, the density perturbation manifests as crosstalk in the estimated *P*- and *S*-wave velocity perturbation images. It is clear that the results will impede the proper interpretation of the *P*- and *S*-wave images. The proposed three-parameter elastic LSRTM can suppress the crosstalk (Figs 4a, c and e). Moreover, typical RTM artefacts have decreased and the spatial resolution of the images have improved. The number of iterations of the three-parameter elastic LSRTM is 35, and the relative data misfit also reduces to 10 per cent. We also compare the convergence curves of the three-parameter elastic LSRTM and the two-parameter elastic LSRTM (Fig. 5). Including density perturbation in the inversion leads to an improvement in the convergence of the iterative inversion.

Elastic Marmousi2 model

In this section, we evaluate the proposed algorithm on a more complex model: the elastic Marmousi2 model (Martin *et al.* 2006). We reduce the size of the original model to 1001 × 426 grids with grid interval 2.5 m. We also replace the water layer by a low-velocity layer in the original model. Figs 6(a), (c) and (e) show the true *P*- and *S*-wave velocity and density models. There are uncorrelated structures in the three models (indicated by the white triangles) representing potential hydrocarbon reservoirs. There are 101 shots located along the surface of the model with interval of 25 m. There

Downloaded from https://academic.oup.com/gji/article-abstract/216/1/61/5091812 by University of California, Berkeley/LBL user on 21 June 2019

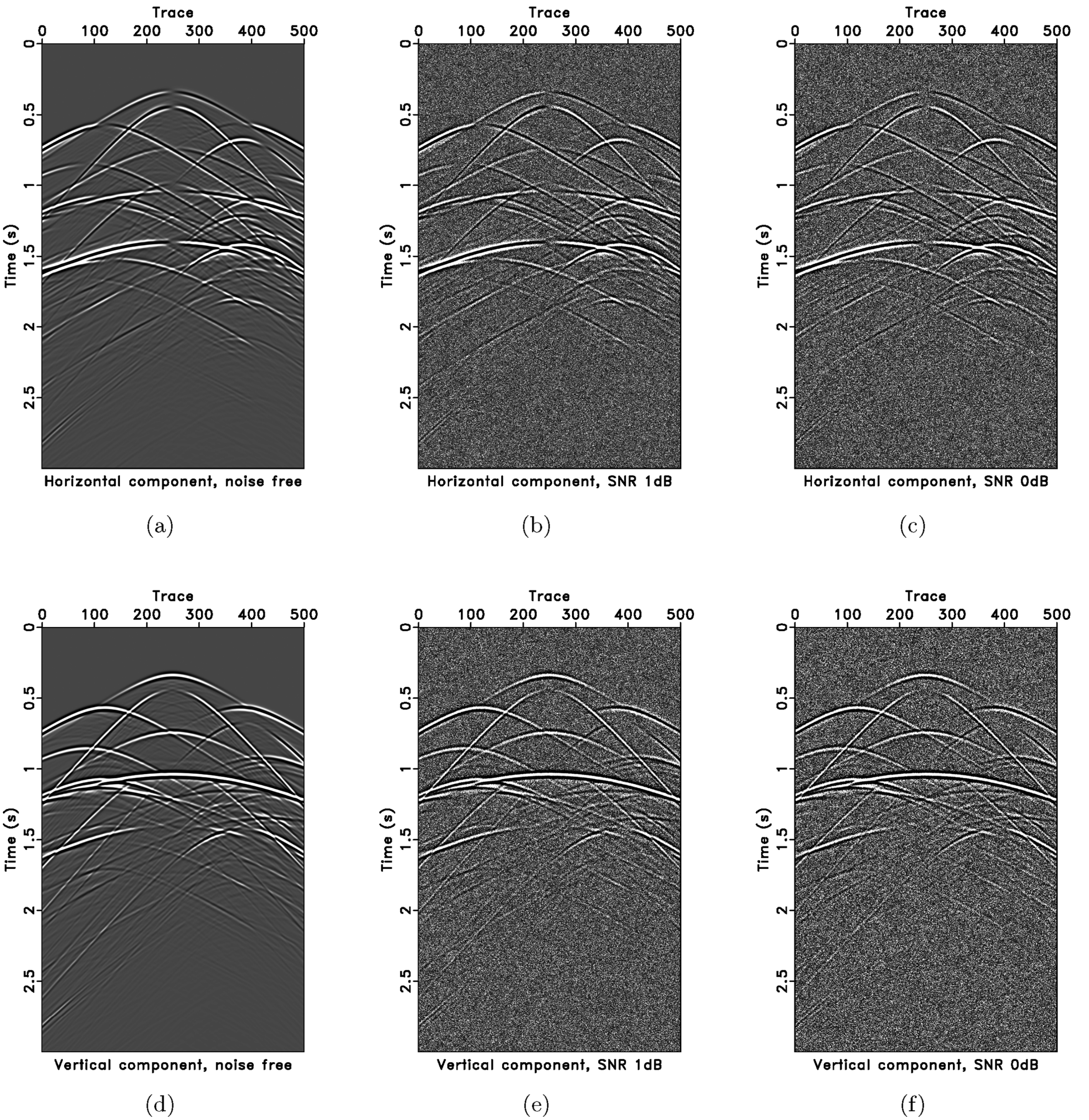

Figure 14. The 50th shot gather with different SNRs. (a) Noise-free horizontal component data. (b) Horizontal component data with SNR 1 dB. (c) Horizontal component data with SNR 0 dB. (d) Noise-free vertical component data. (e) Vertical component data with SNR 1 dB. (f) Vertical component data with SNR 0 dB.

are 1001 receivers located along the surface of the model with interval of 2.5 m. The source wavelet is a Ricker wavelet with central frequency 35 Hz. The observed data are simulated using our time-domain elastic FD code (Fig. 7). The data contain full-wave modes except for direct waves. Figs 6(b), (d) and (f) are the smoothed background *P*- and *S*-wave velocity and density models. Background model smoothing is obtained by convolving the true models with a 2-D Gaussian filter of 35 m width. Figs 8(a), (c) and (e) show the true *P*- and *S*-wave velocity and density perturbations.

The images generated by elastic RTM contain strong low-frequency RTM artefacts (Figs 8b, d and f). Moreover, the amplitudes for the shallow and deep parts of the images are unbalanced. A particular issue is that the elastic RTM generates crosstalk among the three elastic images in areas where the models are uncorrelated. The two-parameter elastic LSRTM (Chen & Sac-

Downloaded from https://academic.oup.com/gji/article-abstract/216/1/61/5091812 by University of California, Berkeley/LBL user on 21 June 2019

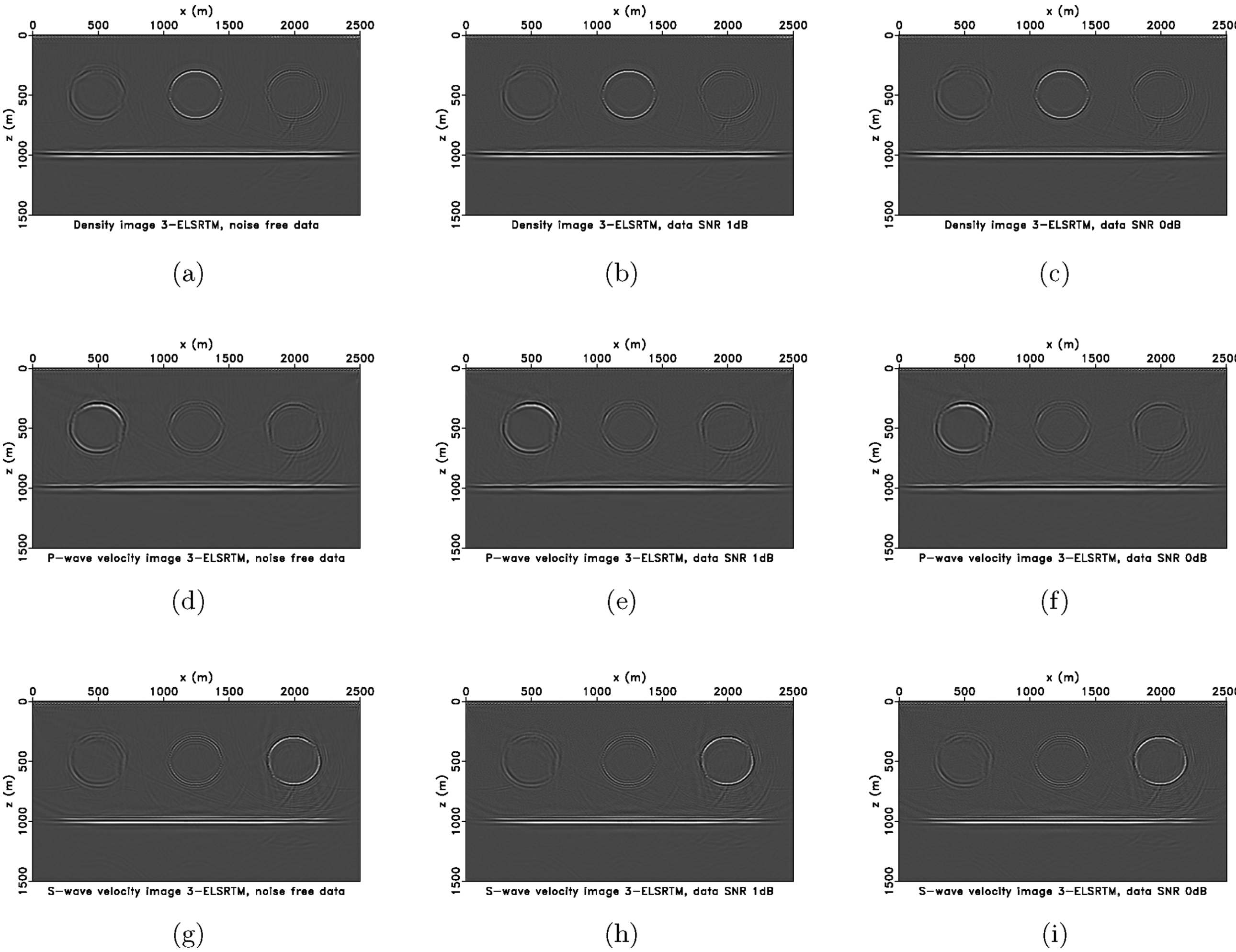

Figure 15. Three-parameter elastic LSRTM images using data with different SNRs. Estimated density images from noise-free data (a), data with SNR 1 dB (b) and data with SNR 0 dB (c). Estimated *P*-wave velocity images from noise-free data (d), data with SNR 1 dB (e) and data with SNR 0 dB (f). Estimated *S*-wave velocity images from noise-free data (g), data with SNR 1 dB (h) and data with SNR 0 dB (i).

chi 2017) can largely resolve those problems (Figs 9b and d). However, it does not provide an estimation of the density perturbation image. These results were obtained after 100 iterations of the two-parameter elastic LSRTM. And the relative data misfit reduces to about 40 per cent. The proposed three-parameter elastic LSRTM is able to estimate the *P*- and *S*-wave velocity and density perturbation images (Figs 9a, c and e). The images have more balanced amplitudes, fewer low-frequency RTM artefacts and reduced multiparameter crosstalk. These results were obtained after 100 iterations of the three-parameter elastic LSRTM. And the relative data misfit reduces to about 23 per cent. To appreciate details more clearly, we compare the elastic images in the three windows around the three white triangles in the model (Figs 6a, c and e) as Figs 10, 11 and 12. The three-parameter elastic LSRTM generated images with highest spatial resolution and fewest artefacts and crosstalk. We compare the convergence curves of the three-parameter elastic LSRTM and two-parameter elastic LSRTM in Fig. 13. The three-parameter elastic LSRTM converges faster than the two-parameter elastic LSRTM.

The effect of noise

In this section, we investigate the effect of noise on results of the elastic LSRTM. We generate the noise as follows. For each shot gather, a random noise gather is generated following a standard normal distribution. Then, the noise gather is filtered at the maximum frequency band of the data (Blom *et al.* 2017). Finally, the filtered noise gather is scaled to a predefined signal-to-noise ratio (SNR). The SNR in decibels (dB) for a shot gather is defined as

$$\mathrm{SNR} = 10 \log_{10} \left(\frac{A_{\mathrm{s}}}{A_{\mathrm{n}}} \right)^2, \tag{19}$$

where A_{s} and A_{n} are the root-mean-square amplitudes of signal and noise in the shot gather, respectively. Fig. 14 shows the 50th shot gather with different SNRs for the elastic inclusion model example. Fig. 15 shows the estimated density, *P*- and *S*-wave velocity images by three-parameter elastic LSRTM (after 35 iterations) using data with different SNRs. Fig. 16 shows the 50th shot gather with different SNRs for the elastic Marmousi2 model example. Fig. 17

Downloaded from https://academic.oup.com/gji/article-abstract/216/1/61/5091812 by University of California, Berkeley/LBL user on 21 June 2019

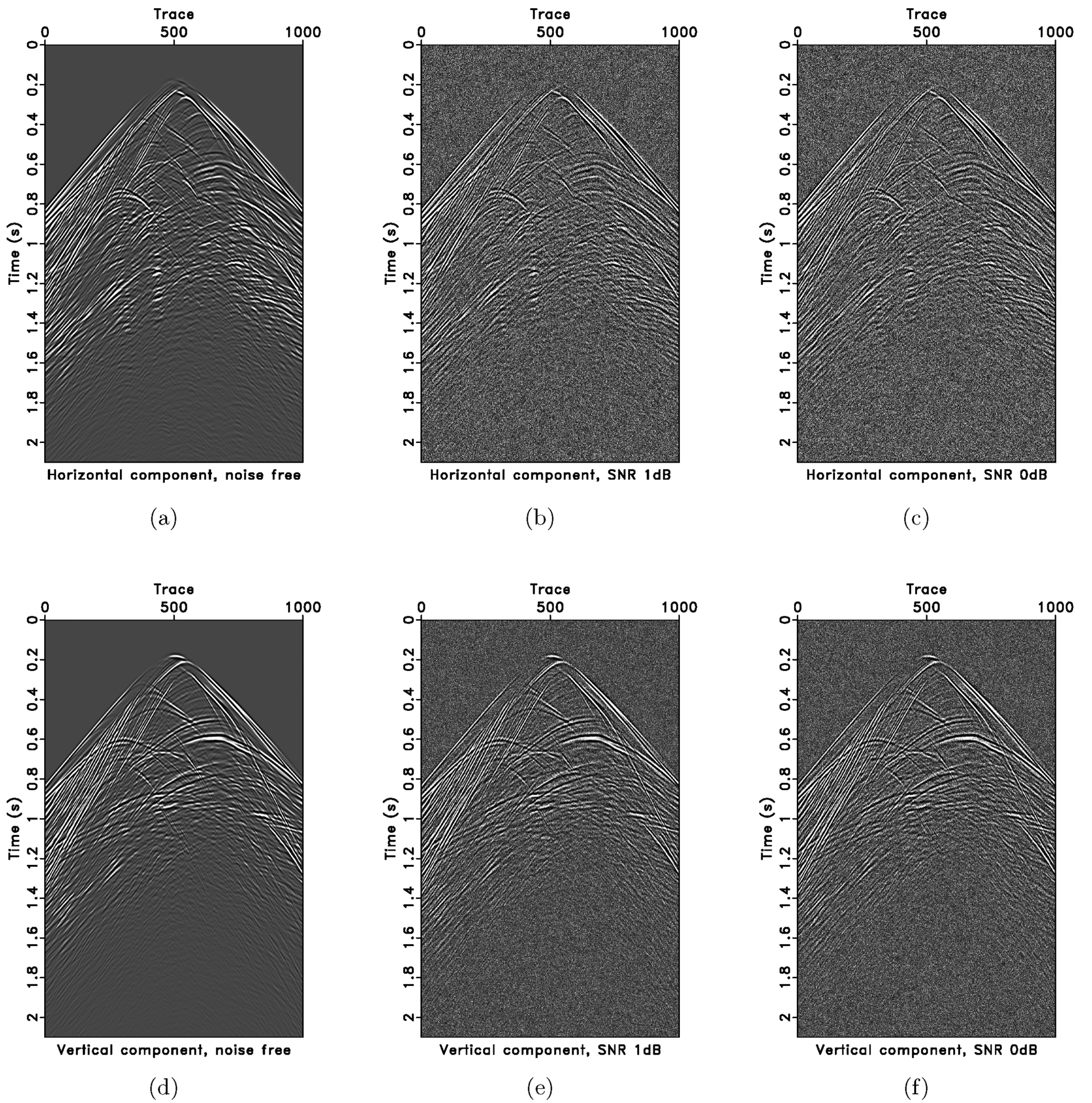

Figure 16. The 50th shot gather with different SNRs. (a) Noise-free horizontal component data. (b) Horizontal component data with SNR 1 dB. (c) Horizontal component data with SNR 0 dB. (d) Noise-free vertical component data. (e) Vertical component data with SNR 1 dB. (f) Vertical component data with SNR 0 dB.

shows the corresponding recovered images by three-parameter elastic LSRTM (after 100 iterations). The results from noisy data and noise-free data are roughly similar. The presence of data noise deteriorates the estimated images. The data noise leads to noise artefacts in the recovered images. As mentioned in previous sections, the Laplacian filter has been applied on the migration/inverted images to remove the high-amplitude low-frequency RTM artefacts. It will also reduce the amount of noise artefacts generated from data noise.

DISCUSSION

In this paper, the resolution of images is referred to as the spatial resolution. It is the minimum distance between two point scatters

Downloaded from https://academic.oup.com/gji/article-abstract/216/1/61/5091812 by University of California, Berkeley/LBL user on 21 June 2019

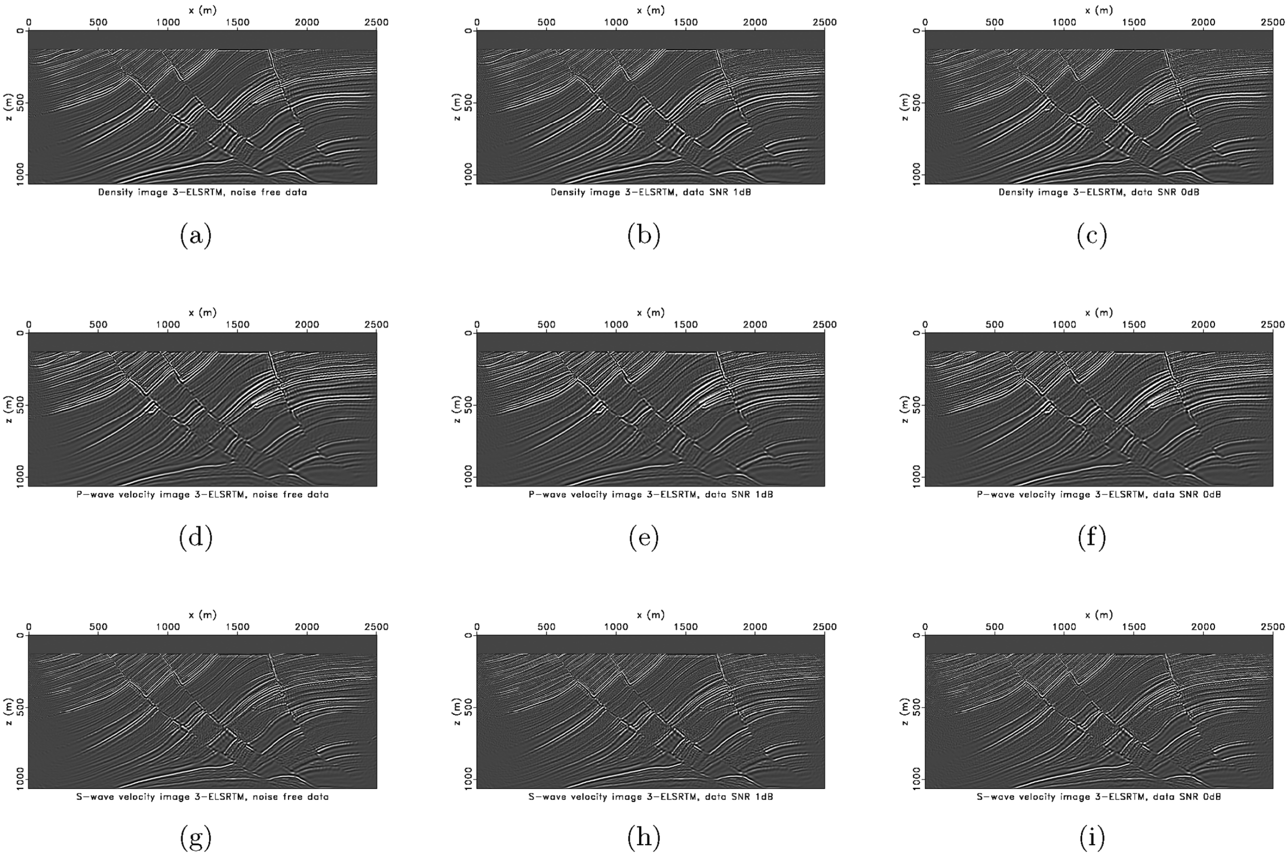

Figure 17. Three-parameter elastic LSRTM images using data with different SNRs. Estimated density images from noise-free data (a), data with SNR 1 dB (b) and data with SNR 0 dB (c). Estimated *P*-wave velocity images from noise-free data (d), data with SNR 1 dB (e) and data with SNR 0 dB (f). Estimated *S*-wave velocity images from noise-free data (g), data with SNR 1 dB (h) and data with SNR 0 dB (i).

that can be resolved in the migrated/inverted section (Safar 1985; Schuster *et al.* 2017). The spatial resolution can be specified in terms of vertical and lateral resolution (Berkhout & Van Wulfften Palthe 1979). The spatial resolution limit of migration algorithms depends on the seismic experiment configuration (acquisition aperture and source bandwidth), migration/inversion algorithm used and the initial background model (Beylkin *et al.* 1985; Levin 1998).

The resolution of model parameters in an inverse problem can also be quantified. Quantitative resolution analysis of LSM algorithms can be performed based on resolution matrix (Berryman 1994a,b; Zhang & McMechan 1995; Minkoff 1996; Yao *et al.* 1999; Fomel *et al.* 2002; Zhang & Thurber 2007; Song *et al.* 2011), point spreading function (Humphreys & Clayton 1988; Alumbaugh & Newman 2000; Oldenborger & Routh 2009) and Hessian (Fichtner & Trampert 2011; Fichtner & Leeuwen 2015).

When the background migration model is good enough, the density image estimated by elastic LSRTM can be linked to rock properties and help quantitive interpretation. It is worth to mention that the density–velocity trade-off has been investigated in the field of waveform inversion (Cara *et al.* 1984; Tanimoto 1991; Kohn *et al.* 2012; Płonka *et al.* 2016; Blom *et al.* 2017; Koelemeijer *et al.* 2017; Pan *et al.* 2018).

CONCLUSIONS

The conventional two-parameter elastic LSRTM algorithm does not consider density image in the inversion. Neglecting density image in the inversion may generate crosstalk artefacts in *P*- and *S*-wave images. We propose a time-domain three-parameter elastic LSRTM method. It simultaneously invert for density, *P*- and *S*-wave velocity perturbation images. We derive the elastic Born approximation and elastic RTM operators using the time-domain continuous adjoint-state method. We carefully discretize the two operators to assure that they pass the dot-product test. The latter allows us to use the CGLS method to solve the LSM quadratic optimization problem on the fly. We observe that the proposed three-parameter elastic LSRTM can decouple the three isotropic elastic parameters and suppress the crosstalk. Moreover, it provides faster convergence and an improved data fitting than the two-parameter elastic LSRTM.

ACKNOWLEDGEMENTS

We thank the editor Herve Chauris, reviewer Andreas Fichtner and reviewer Daniel Trad for their valuable suggestions and comments that improved the manuscript. We thank the sponsors of the Signal Analysis and Imaging Group (SAIG) at the University of Alberta for financial support. This research was also supported by the Natural Sciences and Engineering Research Council of Canada (NSERC) via a Discovery Grant to MDS. Compute Canada provided high-performance clustered computing resources. Figures in this paper were plotted using the Madagascar open-source software package.

Downloaded from https://academic.oup.com/gji/article-abstract/216/1/61/5091812 by University of California, Berkeley/LBL user on 21 June 2019

REFERENCES

Alumbaugh, D.L. & Newman, G.A., 2000. Image appraisal for 2-D and 3-D electromagnetic inversion, *Geophysics,* **65**(5), 1455–1467.

Anikiev, D., Kashtan, B. & Mulder, W.A., 2013. Decoupling of elastic parameters with iterative linearized inversion, in *83rd Annual International Meeting,* SEG, Expanded Abstracts, pp. 3185–3190, Houston, TX.

Baysal, E., Kosloff, D.D. & Sherwood, J.W.C., 1983. Reverse time migration, *Geophysics,* **48**(11), 1514–1524.

Berkhout, A.J. & Van Wulfften Palthe, D.W., 1979. Migration in terms of spatial deconvolution, *Geophys. Prospect.,* **27**(1), 261–291.

Berryman, J.G., 1994a. Resolution of iterative inverses in seismic tomography, in *Proceedings of the Cornelius Lanczos International Centenary Conference,* pp. 297–299, eds Brown, J.D., Chu, M.T., Ellison, D.C. & Plemmons, R.J., SIAM.

Berryman, J.G., 1994b. Tomographic resolution without singular value decomposition, *Proc. SPIE,* **2301,** 2–13.

Beydoun, W.B. & Mendes, M., 1989. Elastic ray-Born l_2-migration/inversion, *Geophys. J. Int.,* **97**(1), 151–160.

Beylkin, G., Oristaglio, M. & Miller, D., 1985. Spatial resolution of migration algorithms, in *Acoustical Imaging,* pp. 155–167, eds Berkhout, A.J., Ridder, J. & van der Wal, L.F., Springer.

Bjorck, A., 1996. *Numerical Methods for Least Squares Problems,* Society for Industrial and Applied Mathematics.

Blom, N., Boehm, C. & Fichtner, A., 2017. Synthetic inversions for density using seismic and gravity data, *Geophys. J. Int.,* **209**(2), 1204–1220.

Bourgeois, A., Jiang, B.F. & Lailly, P., 1989. Linearized inversion: a significant step beyond pre-stack migration, *Geophys. J. Int.,* **99**(2), 435–445.

Cara, M., Leveque, J.J. & Maupin, V., 1984. Density-versus-depth models from multimode surface waves, *Geophys. Res. Lett.,* **11**(7), 633–636.

Chang, W. & McMechan, G.A., 1987. Elastic reverse-time migration, *Geophysics,* **52**(10), 1365–1375.

Chen, K. & Sacchi, M.D., 2017. Elastic least-squares reverse time migration via linearized elastic full-waveform inversion with pseudo-Hessian preconditioning, *Geophysics,* **82**(5), S341–S358.

Chen, P. & Lee, E.-J., 2015. *Full-3D Seismic Waveform Inversion,* Springer Geophysics.

Chen, Y., Chen, H., Xiang, K. & Chen, X., 2017. Preserving the discontinuities in least-squares reverse time migration of simultaneous-source data, *Geophysics,* **82,** S185–S196.

Cheng, J., Kazemi, N. & Sacchi, M., 2016. Least-squares migration via a gradient projection method - application to seismic data deblending, in *78th Annual International Conference and Exhibition,* EAGE, Extended Abstracts, doi:10.3997/2214-4609.201601413.

Claerbout, J.F., 1985. *Imaging the Earth's Interior,* Blackwell Scientific Publications.

Claerbout, J.F., 1992. *Earth Soundings Analysis: Processing versus Inversion,* Blackwell Scientific Publications.

Dai, W., Fowler, P. & Schuster, G.T., 2012. Multi-source least-squares reverse time migration, *Geophys. Prospect.,* **60,** 681–695.

Du, Q., Zhu, Y. & Ba, J., 2012. Polarity reversal correction for elastic reverse time migration, *Geophysics,* **77**(2), S31–S41.

Duan, Y., Guitton, A. & Sava, P., 2017. Elastic least-squares reverse time migration, *Geophysics,* **82**(4), S315–S325.

Dussaud, E., Symes, W.W., Williamson, P., Lemaistre, L., Singer, P., Denel, B. & Cherrett, A., 2008. Computational strategies for reverse-time migration, in *78th Annual International Meeting,* SEG, Expanded Abstracts, pp. 2267–2271, Las Vegas, NV.

Dong, S., Cai, J., Guo, M., Suh, S., Zhang, Z., Wang, B. & Li, Z., 2012. Least-squares reverse time migration: towards true amplitude imaging and improving the resolution, in *82nd Annual International Meeting,* SEG, Expanded Abstracts, 1–5, Las Vegas, NV.

Etgen, J., Gray, S.H. & Zhang, Y., 2009. An overview of depth imaging in exploration geophysics, *Geophysics,* **74**(6), WCA5–WCA17.

Etgen, J.T., 1986. Prestack reverse time migration of shot profiles, SEP-50, pp. 151–169.

Feng, Z. & Schuster, G.T., 2017. Elastic least-squares reverse time migration, *Geophysics,* **82**(2), S143–S157.

Fichtner, A., 2010. *Full Seismic Waveform Modelling and Inversion,* Springer.

Fichtner, A. & Leeuwen, T.V., 2015. Resolution analysis by random probing, *J. geophys. Res.,* **120**(8), 5549–5573.

Fichtner, A. & Trampert, J., 2011. Resolution analysis in full waveform inversion, *Geophys. J. Int.,* **187**(3), 1604–1624.

Fichtner, A., Bunge, H.-P. & Igel, H., 2006a. The adjoint method in seismology: I. Theory, *Phys. Earth planet. Inter.,* **157**(1–2), 86–104.

Fichtner, A., Bunge, H.-P. & Igel, H., 2006b. The adjoint method in seismology: II. Applications: traveltimes and sensitivity functionals, *Phys. Earth planet. Inter.,* **157**(1), 105–123.

Fomel, S., Berryman, J.G., Clapp, R.G. & Prucha, M., 2002. Iterative resolution estimation in least-squares Kirchhoff migration, *Geophys. Prospect.,* **50**(6), 577–588.

Gauthier, O., Virieux, J. & Tarantola, A., 1986. Two-dimensional nonlinear inversion of seismic waveforms: numerical results, *Geophysics,* **51**(7), 1387–1403.

Gu, B., Li, Z., Yang, P., Xu, W. & Han, J., 2017. Elastic least-squares reverse time migration with hybrid $l1/l2$ misfit function, *Geophysics,* **82**(3), S271–S291.

Guo, P. & McMechan, G.A., 2018. Compensating Q effects in viscoelastic media by adjoint-based least-squares reverse time migration, *Geophysics,* **83**(2), S151–S172.

Hestenes, M.R. & Stiefel, E., 1952. Methods of conjugate gradients for solving linear systems, *J. Res. Natl. Bur. Stand.,* **49**(6), 409–436.

Hou, J. & Symes, W.W., 2016. Accelerating extended least-squares migration with weighted conjugate gradient iteration, *Geophysics,* **81,** S165–S179.

Humphreys, E. & Clayton, R.W., 1988. Adaptation of back projection tomography to seismic travel time problems, *J. geophys. Res.,* **93**(B2), 1073–1085.

Jin, S., Madariaga, R., Virieux, J. & Lambaré, G., 1992. Two-dimensional asymptotic iterative elastic inversion, *Geophys. J. Int.,* **108**(2), 575–588.

Kaplan, S.T., Routh, P.S. & Sacchi, M.D., 2010. Derivation of forward and adjoint operators for least-squares shot-profile split-step migration, *Geophysics,* **75**(6), S225–S235.

Kazemi, N. & Sacchi, M.D., 2015. Block row recursive least-squares migration, *Geophysics,* **80**(5), A95–A101.

Koelemeijer, P., Deuss, A. & Ritsema, J., 2017. Density structure of Earth's lowermost mantle from Stoneley mode splitting observations, *Nat. Commun.,* **8**.

Kohn, D., De Nil, D., Kurzmann, A., Przebindowska, A. & Bohlen, T., 2012. On the influence of model parametrization in elastic full waveform tomography, *Geophys. J. Int.,* **191**(1), 325–345.

Komatitsch, D. & Martin, R., 2007. An unsplit convolutional perfectly matched layer improved at grazing incidence for the seismic wave equation, *Geophysics,* **72**(5), SM155–SM167.

Kuehl, H. & Sacchi, M.D., 2003. Least-squares wave-equation migration for AVP/AVA inversion, *Geophysics,* **68**(1), 262–273.

Li, Y. & Chauris, H., 2017. An alternative true-amplitude common-shot reverse time migration, in *79th EAGE Conference and Exhibition,* Extended Abstracts, doi:10.3997/2214-4609.201701364.

Lambare, G., Virieux, J., Madariaga, R. & Jin, S., 1992. Iterative asymptotic inversion in the acoustic approximation, *Geophysics,* **57**(9), 1138–1154.

Levin, S.A., 1998. Resolution in seismic imaging: is it all a matter of perspective?, *Geophysics,* **63**(2), 743–749.

Lions, J.L., 1971. *Optimal Control of Systems Governed by Partial Differential Equations,* Springer.

Liu, Y. & Sen, M.K., 2009. An implicit staggered-grid finite-difference method for seismic modelling, *Geophys. J. Int.,* **179**(1), 459–474.

Martin, G.S., Wiley, R. & Marfurt, K.J., 2006. Marmousi2: an elastic upgrade for Marmousi, *Leading Edge,* **25**(2), 156–166.

McMechan, G.A., 1983. Migration by extrapolation of time-dependent boundary values, *Geophys. Prospect.,* **31**(3), 413–420.

Minkoff, S.E., 1996. A computationally feasible approximate resolution matrix for seismic inverse problems, *Geophys. J. Int.,* **126**(2), 345–359.

Nemeth, T., Wu, C. & Schuster, G.T., 1999. Least-squares migration of incomplete reflection data, *Geophysics,* **64**(1), 208–221.

Downloaded from https://academic.oup.com/gji/article-abstract/216/1/61/5091812 by University of California, Berkeley/LBL user on 21 June 2019

Oldenborger, G.A. & Routh, P.S., 2009. The point-spread function measure of resolution for the 3-D electrical resistivity experiment, *Geophys. J. Int.,* **176**(2), 405–414.

Ostmo, S., Mulder, W.A. & Plessix, R.-. 2002. Finite-difference iterative migration by linearized waveform inversion in the frequency domain, in *72nd Annual International Meeting,* SEG, Expanded Abstracts, pp. 1384–1387, Salt Lake City, UT.

Operto, S., Gholami, Y., Prieux, V., Ribodetti, A., Brossier, R., Metivier, L. & Virieux, J., 2013. A guided tour of multiparameter full-waveform inversion with multicomponent data: from theory to practice, *Leading Edge,* **32**(9), 1040–1054.

Pageot, D., Operto, S., Valle, M., Brossier, R. & Virieux, J., 2013. A parametric analysis of two-dimensional elastic full waveform inversion of teleseismic data for lithospheric imaging, *Geophys. J. Int,* **193,** 1479–1505.

Paige, C.C. & Saunders, M.A., 1982. LSQR: an algorithm for sparse linear equations and sparse least squares, *ACM Trans. Math. Softw.,* **8**(1), 43–71.

Pan, W., Geng, Y. & Innanen, K.A., 2018. Interparameter trade-off quantification and reduction in isotropic-elastic full-waveform inversion: synthetic experiments and Hussar land data set application, *Geophys. J. Int.,* **213**(2), 1305–1333.

Plessix, R.-E., 2006. A review of the adjoint-state method for computing the gradient of a functional with geophysical applications, *Geophys. J. Int.,* **167**(2), 495–503.

Płonka, A., Blom, N. & Fichtner, A., 2016. The imprint of crustal density heterogeneities on regional seismic wave propagation, *Solid Earth,* **7**(6), 1591–1608.

Qu, Y., Li, J., Huang, J. & Li, Z., 2018. Elastic least-squares reverse time migration with velocities and density perturbation, *Geophys. J. Int.,* **212**(2), 1033–1056.

Ren, Z., Liu, Y. & Sen, M.K., 2017. Least-squares reverse time migration in elastic media, *Geophys. J. Int.,* **208**(2), 1103–1125.

Rickett, J.E., 2003. Illumination-based normalization for wave-equation depth migration, *Geophysics,* **68**(4), 1371–1379.

Safar, M.H., 1985. On the lateral resolution achieved by Kirchhoff migration, *Geophysics,* **50**(7), 1091–1099.

Schuster, G.T., Dutta, G. & Li, J., 2017. Resolution limits of migration and linearized waveform inversion images in a lossy medium, *Geophys. J. Int.,* **209**(3), 1612–1621.

Song, X., Baumstein, A. & Routh, P., 2011. Resolution analysis for full wavefield inversion and its application to time-lapse, in *81st Annual International Meeting,* SEG, Expanded Abstracts, pp. 2597–2602, San Antonio, TX.

Stanton, A. & Sacchi, M., 2015. Least squares wave equation migration of elastic data, in *77th Annual International Conference and Exhibition,* EAGE, Extended Abstracts, doi:10.3997/2214-4609.201412706.

Stanton, A. & Sacchi, M.D., 2017. Elastic least-squares one-way wave-equation migration, *Geophysics,* **82**(4), S293–S305.

Sun, M., Dong, L., Liu, Y. & Yang, J., 2017. The least-squares elastic reverse-time migration with density variation, in *79th Annual International Conference and Exhibition,* EAGE, Extended Abstracts, doi:10.3997/2214-4609.201701128.

Sun, R. & McMechan, G.A., 1986. Pre-stack reverse-time migration for elastic waves with application to synthetic offset vertical seismic profiles, *Proc. IEEE,* **74**(3), 457–465.

Sun, R. & McMechan, G.A., 2001. Scalar reverse-time depth migration of prestack elastic seismic data, *Geophysics,* **66**(5), 1519–1527.

Tang, Y., 2009. Target-oriented wave-equation least-squares migration/inversion with phase-encoded Hessian, *Geophysics,* **74**(6), WCA95–WCA107.

Tanimoto, T., 1991. Waveform inversion for three-dimensional density and *S* wave structure, *J. geophys. Res.,* **96**(B5), 8167–8189.

Tarantola, A., 1984. Linearized inversion of seismic reflection data, *Geophys. Prospect.,* **32**(6), 998–1015.

Tarantola, A., 1986. A strategy for nonlinear elastic inversion of seismic reflection data, *Geophysics,* **51**(10), 1893–1903.

Tarantola, A., 1988. Theoretical background for the inversion of seismic waveforms, including elasticity and attenuation, in *Scattering and Attenuations of Seismic Waves,* pp. 365–399, eds Aki, K. & Wu, R.-S., Birkhäuser.

Trad, D., 2015. Least squares Kirchhoff depth migration: implementation, challenges, and opportunities, in *85th Annual International Meeting,* SEG, Expanded Abstracts, pp. 4238–4242, New Orleans, LA.

Trad, D., 2017. Challenges for least-squares Kirchhoff depth migration, in *87th Annual International Meeting,* SEG, Expanded Abstracts, pp. 4545–4549, Houston, TX.

Tromp, J., Tape, C. & Liu, Q., 2005. Seismic tomography, adjoint methods, time reversal and banana-doughnut kernels, *Geophys. J. Int.,* **160**(1), 195–216.

Virieux, J., 1986. *P-SV* wave propagation in heterogeneous media: velocity-stress finite-difference method, *Geophysics,* **51**(4), 889–901.

Wang, J., Kuehl, H. & Sacchi, M.D., 2005. High-resolution wave-equation AVA imaging: algorithm and tests with a data set from the Western Canadian Sedimentary Basin, *Geophysics,* **70**(5), S91–S99.

Whitmore, N.D., 1983. Iterative depth migration by backward time propagation, in *53rd Annual International Meeting,* SEG, Expanded Abstracts, pp. 382–385, Las Vegas, NV.

Xu, L. & Sacchi, M.D., 2018. Preconditioned acoustic least-squares two-way wave equation migration with exact adjoint operator, *Geophysics,* **83,** S1–S13.

Xu, L., Stanton, A. & Sacchi, M., 2016. Elastic least-squares reverse time migration, in *86th Annual International Meeting,* SEG, Expanded Abstracts, pp. 2289–2293, Dallas, TX.

Xue, Z., Chen, Y., Fomel, S. & Sun, J., 2016. Seismic imaging of incomplete data and simultaneous-source data using least-squares reverse time migration with shaping regularization, *Geophysics,* **81,** S11–S20.

Yan, J. & Sava, P., 2008. Isotropic angle-domain elastic reverse-time migration, *Geophysics,* **73**(6), S229–S239.

Yang, J., Liu, Y. & Dong, L., 2016. Least-squares reverse time migration in the presence of density variations, *Geophysics,* **81,** S497–S509.

Yao, G. & Jakubowicz, H., 2016. Least-squares reverse-time migration in a matrix-based formulation, *Geophys. Prospect.,* **64,** 611–621.

Yao, Z.S., Roberts, R.G. & Tryggvason, A., 1999. Calculating resolution and covariance matrices for seismic tomography with the LSQR method, *Geophys. J. Int.,* **138**(3), 886–894.

Zhang, H. & Thurber, C.H., 2007. Estimating the model resolution matrix for large seismic tomography problems based on lanczos bidiagonalization with partial reorthogonalization, *Geophys. J. Int.,* **170**(1), 337–345.

Zhang, J. & McMechan, G.A., 1995. Estimation of resolution and covariance for large matrix inversions, *Geophys. J. Int.,* **121**(2), 409–426.

Zhang, Y. & Sun, J., 2009. Practical issues in reverse time migration: true amplitude gathers, noise removal and harmonic source encoding, *First Break,* **27,** 53–59.

Zhang, Y., Duan, L. & Xie, Y., 2015. A stable and practical implementation of least-squares reverse time migration, *Geophysics,* **80,** V23–V31.

Downloaded from https://academic.oup.com/gji/article-abstract/216/1/61/5091812 by University of California, Berkeley/LBL user on 21 June 2019